

TAKYI-ANINAKWA, P., WANG, S., ZHANG, H., YANG, X. and FERNANDEZ, C. 2022. An optimized long short-term memory-weighted fading extended Kalman filtering model with wide temperature adaptation for the state of charge estimation of lithium-ion batteries. *Applied energy* [online], 326, article 120043. Available from: <https://doi.org/10.1016/j.apenergy.2022.120043>

# An optimized long short-term memory-weighted fading extended Kalman filtering model with wide temperature adaptation for the state of charge estimation of lithium-ion batteries.

TAKYI-ANINAKWA, P., WANG, S., ZHANG, H., YANG, X. and FERNANDEZ, C.

2022

© 2022 Elsevier Ltd.

## **An optimized long short-term memory-weighted fading extended Kalman filtering model with wide temperature adaptation for the state of charge estimation of lithium-ion batteries**

Paul Takyi-Aninakwa<sup>a</sup>, Shunli Wang<sup>a,\*</sup>, Hongying Zhang<sup>a</sup>, Xiaoyong Yang<sup>a</sup>, Carlos Fernandez<sup>b</sup>

a School of Information Engineering, Southwest University of Science and Technology, Mianyang 621010, China

b School of Pharmacy and Life Sciences, Robert Gordon University, Aberdeen AB10-7GJ, UK

### **ABSTRACT**

Accurate state of charge (SOC) estimation at different operating temperatures is essential for the reliable and safe operation of battery management systems (BMS) for lithium-ion batteries in electric vehicles (EVs). In this paper, an optimized long-short-term memory-weighted fading extended Kalman filtering (LSTM-WFEKF) model with wide temperature adaptation is proposed as a temperature-conditioned model for SOC estimation. Firstly, the input datasets are categorized based on the operating temperatures for EVs in the United States Advanced Battery Consortium manual: cold ( $-10^{\circ}\text{C}$ ), normal ( $25^{\circ}\text{C}$ ), and hot ( $50^{\circ}\text{C}$ ) temperatures and optimized with an attention mechanism for faster training of the LSTM model to cross-train and test to specifically study the effects of temperature on the SOC estimation through a transfer learning mechanism. Secondly, the SOC estimated by the LSTM model is input into a WFEKF method, which introduces adaptive weighing and fading factors to correct, denoise, and optimize the final SOC for each temperature variation under complex working conditions. Finally, the results show that the training and testing temperatures have distinctive SOC effects using the LSTM model. Also, the proposed LSTM-WFEKF model estimates the SOC with overall best mean absolute error (MAE), root mean square error (RMSE), and R-squared (R<sup>2</sup>) values of 0.0697%, 0.0784%, and 99.9965%, respectively, under different temperatures and complex working conditions, which is optimal compared to other existing models. Based on the MAE, RMSE, and R<sup>2</sup> values under different operating temperatures and complex working conditions, this paper concludes that the  $25^{\circ}\text{C}$  training dataset ensures a more accurate SOC estimation. Meanwhile, the  $-10^{\circ}\text{C}$  and  $50^{\circ}\text{C}$  training datasets cause more and less noisy estimates, respectively. The proposed LSTM-WFEKF model has wide temperature and working condition adaptability for real-time BMS applications in EVs.

Abbreviations: ADAM, Adaptive moment estimate; Ah, Ampere-hour integration method; BBDST, Beijing bus dynamic stress test; BMS, Battery management system; CC, Constant current; CNN, Convolutional neural network; CV, Constant voltage; DL, Deep learning; DST, Dynamic stress test; ECM, Equivalent circuit model; EV, Electric vehicle; FUDS, Federal urban driving cycle; GRU, Gated recurrent unit; HPPC, Hybrid pulse power characterization; HWFET, Highway fuel economy test; IFO, Improved fractional order; LNCM, Lithium nickel cobalt manganese; LSTM, Long short-term memory; MAE, Mean absolute error; ME, Maximum error; ML, Machine learning; NEDC, New European driving cycle; OCV, Open-circuit voltage; PSO, Particle swarm optimization; R<sup>2</sup>, R-squared; RMSE, Root mean squared error; RNN, Recurrent neural network; RT, Room temperature; SOC, State of charge; TL, Transfer learning; UDDS, Urban dynamometer driving schedule; USABC, United States Advanced Battery Consortium; WFEKF, Weighted fading extended Kalman filter.

## **Introduction**

Lithium-ion batteries have gradually become the most promising system for power storage in smart devices, e-bikes, electric tools, hoverboards, electric vehicles (EVs), spacecraft, and solar power backup systems. Compared to other rechargeable batteries (nickel–cadmium, nickel-metal hydride, lead-acid, etc.), lithium-ion batteries are preferred due to their appreciable advantages, such as high specific energy, high energy density, no memory effect, low self-discharge rate, longevity, wide operating temperatures, etc. [1–3]. However, due to the high nonlinearities, such as aging degree, temperature, over-charge, over-discharge, etc., encountered during the operation of lithium-ion batteries, an accurate state of charge (SOC) estimation is highly essential [4]. The term “SOC estimation” refers to the ability of the battery management system (BMS) to functionally determine the available capacity of the battery [5,6]. Equivalent to fuel gauges in internal combustion engine vehicles, the SOC indicates the total energy remaining in the batteries of battery, hybrid, and plug-in EVs and other smart devices [2,7]. The BMS requires accurate SOC not only for EV range calculation and trip preparation but also to maximize and guarantee the service life and safety of the battery pack and its users. As a result, one of the key characteristics of the BMS is SOC estimation [8]. The SOC value of the battery is mostly estimated by utilizing some measurable battery parameters, such as current, voltage, etc., and considering the effect of operating temperatures, self-discharge, aging, and other nonlinear factors [9–11].

The methods used for estimating the SOC of the battery can be categorized into four: measurement methods based on characterization parameters, ampere-hour (Ah) integration methods, model-based methods, and data-driven methods. The methods based on characterization parameters include the electrochemical impedance spectroscopy (EIS) method [12] and the open-circuit voltage (OCV) method [13]. The EIS measures the battery’s impedance characteristics over a wide range of frequencies. Even though its implementation is straightforward, it has complex computation and is highly vulnerable to the battery’s state and working conditions [14]. The OCV method estimates the SOC based on the OCV-SOC relationship, but it requires a long rest time for the battery to regain its equilibrium state. Furthermore, its estimates are affected by measurement errors in the OCV value, which makes them unsuitable for onboard applications [15]. For the Ah integration method, its accuracy is susceptible to erroneous initial SOC value and error accumulation during the integration due to load current fluctuations. Also, it is difficult to determine the Coulombic efficiency under different operating conditions [16,17].

For the model-based method, the SOC is estimated based on the characteristic parameters of the battery model established for the state observer. It considers the SOC as a hidden state and constructs a state-space model that associates the SOC with the measured variables, such as current and voltage [8]. Battery models commonly established for model-based methods include the empirical model, electrochemical model, and equivalent circuit model (ECM) to monitor and control the thermodynamic equilibrium potential of the battery [18,19]. Currently, model-based methods include state observers, such as the auto-recursive Kalman filter (KF) [20], extended Kalman filter (EKF) [21], unscented Kalman filter (UKF) [22], particle filter (PF) [23], H-infinity filter [24], and their optimized variants, which have proven to estimate appreciable results [25–29]. These methods exhibit satisfactory robustness against inaccurate SOC initialization and measurement noise. However, it turns out that their performance largely relies on the accuracy of the underlying battery model [8]. Whenever the battery is exposed to complicated load profiles and adverse working conditions, the voltage behavior becomes very difficult to model. As a result, the battery model established for the state observers is often subjected to trial-and-error model parameter identification, resulting in poor SOC estimation and increased computation [30–32].

For the data-driven method, the battery is regarded as a “black box” model rather than a practical mathematical model. This estimation method is model-free, and its performance is highly dependent on the quality of the data with optimal training and hyperparameter selection [33,34]. This model uses feature extraction and sufficient training and testing datasets to directly map the nonlinear correlations between its states and the measured variables, such as current, voltage, temperature, etc. [35,36]. Many nonlinear stresses, such as the current rate, cell aging, operating temperature variations, and other operating conditions that affect the battery, are accounted for in the training and testing process, which are difficult to establish for the model-based estimation methods [30,37]. Several data-driven methods proposed for SOC estimation have served as the most promising methods to overcome the limitations of other existing methods in recent years [38]. Due to their excellent self-adaptation, self-learning, and high estimation accuracy, data-driven methods have been used to accurately estimate the SOC of lithium-ion batteries. Machine learning (ML) models, such as linear regression models [2], support vector machine [36], k-nearest neighbor [39], Gaussian process regression [40], etc., have been proposed for SOC estimation due to their simple estimation process and efficient computation. However, these ML models do not incorporate the high nonlinearities, such as the electrochemical, electrothermal, material degradation, etc., characteristics of the battery under complex working conditions [41]. Also, the accuracy and performance of the ML models heavily depend on the quality and quantity of the input data, and unbalanced datasets lead to overfitting and underfitting problems [42]. On the other hand, the capability of deep learning (DL) models, a type of ML model that automatically maps the complicated and nonlinear temporal correlation between battery data and SOC, has drawn substantial interest in the literature on SOC estimation. DL models such as fully connected neural network (FCNN), convolutional neural network (CNN), and other advanced recurrent neural networks (RNNs), such as long short-term memory (LSTM) and gated recurrent unit (GRU) networks, have greatly expanded by increasing the number of computational layers. They can self-learn their weights and biases using gradient descent methods without any mathematical models, which requires laborious tuning of the parameters [43].

Several DL-based hybrid models have been proposed to address the inherent constraints of the DL models for better SOC estimation of lithium-ion batteries. To estimate the battery’s SOC at room temperature (RT), Fan et al. [44] proposed a hybrid CNN with an ultra-lightweight subspace attention mechanism with a simple recurrent unit (CNNULSAM-SRU) model with key feature processing and transfer mechanism for SOC estimation. Chen et al. [45] proposed a denoising autoencoder (DAE)-GRU model for SOC estimation under three working conditions. The DAE-NN is introduced to extract relevant battery data features at RT. For the estimation of the SOC under noise characterization, Ren et al. [46] presented a hybrid particle swarm optimization (PSO)-LSTM model and compared it with the LSTM model at RT.

However, understanding the effects of the different operating temperatures on lithium-ion batteries is critical in designing the best thermal management systems to minimize thermal runaways during charging and discharging [47]. Several temperature-based DL models have been established for SOC estimation. Ma et al. [41] co-estimated the SOC and state of energy based on the LSTM model under two working conditions: battery chemistry and noise interference at operating temperatures of 0, 10, and 25 °C. Oyewole et al. [48] proposed a controllable deep transfer learning (CDTL) model for the short and long-term estimation of SOC at the early stages of degradation using two LSTM models as the source and target cells at a temperature of 30 °C. Yang et al. [49] used a GRU-RNN model to estimate the SOC at varying operating temperatures ranging from 10 to 50 °C. Tian et al. [50] proposed an LSTM model with an adaptive cubature KF method to achieve accurate and robust SOC estimation of lithium-ion batteries at operating temperatures ranging from 10 to 50 °C under dynamic loading profiles. Bian et al. [51] proposed a computationally complex stacked bidirectional LSTM model for SOC estimation at various operating 3 temperatures of 0, 10, and 25 °C under two working conditions.

Yang et al. [52] proposed an LSTM-RNN model to model the sophisticated battery behavior under varying temperatures for SOC estimation. The estimated SOC is then combined with a UKF method to filter out the noise and reduce the estimation errors at varying temperatures from 10 to 50 °C. Fasahat et al. [53] proposed a model by combining an autoencoder neural network and LSTM for SOC estimation of lithium-ion batteries under two working conditions and temperatures of 0, 25, and 45 °C. Wang et al. [54] proposed an improved GRU-based TL for SOC estimation using small target sample datasets under three working conditions at temperatures ranging from 32–50 °C. Ma et al. [55] proposed a sequence-to-sequence mapping model with a process information (SSMPI) model for SOC estimation by improving the LSTM. It allows the modeling of the state information and the process information with a two-stage pretraining strategy implemented to enhance the feature learning capability of the model at operating temperatures of 0, 25, and 45 °C.

However, understanding the temperature effects on the SOC estimation of lithium-ion batteries plays a significant role in the optimal design, training, and testing using the LSTM model. According to the United States Advanced Battery Consortium (USABC) manual, battery working temperatures for EVs are categorized into cold ( $T \leq -8$  °C), cool ( $-8 < T < 0$  °C), normal ( $20 \pm 10$  °C), warm ( $30 < T < 38$  °C), and hot ( $T \geq 38$  °C) [56,57]. From the existing studies above, it can be observed that none of them cross-trained and tested their models under cold ( $-10$  °C), normal (25 °C), and hot (50 °C) temperatures to specifically study the effects of different training and testing temperatures on the SOC estimation accuracy under different complex working conditions and proposed a robust model to solve the estimation effects, but they estimated the SOC under different temperatures (0–50 °C) and working conditions.

In this paper, a computationally optimized temperature-conditioned LSTM model with wide temperature adaptation is established, which is cross-trained and tested under cold ( $-10$  °C), normal (25 °C), and hot (50 °C) temperatures to specifically study the effects of the training and testing temperatures on the SOC estimation under three complex working conditions through a TL mechanism. Then, a weighted fading extended Kalman filter (WFEKF) method is proposed to denoise and optimize the final SOC effects under different temperatures and working conditions to address the research gap. The training datasets are obtained from battery tests under the hybrid pulse power characterization (HPPC), dynamic stress test (DST), and Beijing bus dynamic stress test (BBDST) working conditions to study the robust deep-learning, generalization ability, and TL accuracy of the LSTM model. The main contributions of this paper are in four folds:

- (1) The cross-trained and tested LSTM model is optimized using an attention mechanism, adaptive moment estimate (ADAM), and optimal hyperparameter selection to solve the long training time and overfitting and improve its generalization ability with accurate SOC estimation under different temperatures and complex working conditions.
- (2) The SOC estimated by the LSTM model is input into the proposed WFEKF method to denoise and optimize the final SOC for each operating temperature variation under complex working conditions. The WFEKF method introduces adaptive weighing and fading factors to recursively correct the posteriori state estimate and error covariance matrix updates of the conventional EKF method.
- (3) The results show that the proposed hybrid LSTM-WFEKF model exhibits quick convergence, low noise, significant optimization, and accurate end-of-discharge error correction ability of the final SOC. Furthermore, it outperforms the LSTM model and other existing temperature-based SOC estimation methods after evaluation using the maximum error (ME), mean absolute error (MAE), root mean square error (RMSE), and R-squared (R2) metrics.

(4) The proposed hybrid model is a data-driven initialized model and does not require an OCV-SOC relationship or an ECM to establish a lookup table under different operating temperatures and working conditions.

The remaining sections of this paper are organized as follows: Section 2 introduces the mathematical analysis: the working principle and architecture of the LSTM model, the training procedure and hyperparameter selection for the LSTM model, the working principle of the WFEKF method; data description and pre-processing; and the flowchart of the LSTM and LSTM-WFEKF models for SOC estimation. Section 3 describes the experimental analysis: the experimental test platform, the BBDST, HPPC, and DST experimental test procedures, SOC estimation results, and the performance evaluation for the LSTM and LSTM-WFEKF models. Section 4 is the conclusion of this paper.

## 2. Mathematical analysis

### 2.1. Working principle and architecture of the LSTM model The RNN is an extension of the feedforward neural network (FNN).

The RNN is an extension of the feedforward neural network (FNN). The colored nodes symbolize the sensitivity of the outputs to the inputs, with a darker shade indicating a higher sensitivity level, as presented in Fig. 1.

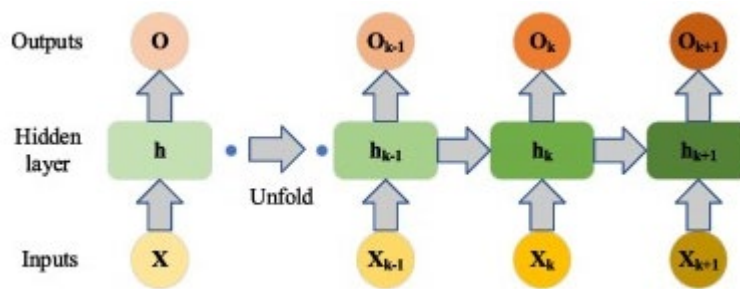


Fig. 1. Basic architecture of the recurrent neural network.

In Fig. 1, the output at time step  $k + 1$  is based on the current input and previous information. This result implies that an RNN can capture pattern recognition in sequential datasets in great detail [50]. However, due to its short-term memory, it cannot solve time-series problems with long-term dependencies caused by the weight in its neurons' transition matrix [58,59].

The LSTM is a practical method for SOC estimation because it considers battery capacity reduction as a time-series problem. Through a memory cell as a gating mechanism, the LSTM precisely simulates the long-term dependencies with its encoder connections to solve the gradient explosion of the conventional RNN. As the characteristic features of the LSTM, the unique memory cell and forgetting modes ensure the model's flexibility to adapt to the arbitrary time-series features of the input during its training [60]. The memory cell maintains and updates information transfers by judging whether they are useful or not throughout its training process [53,61]. The LSTM uses three gates to protect and control the memory cell, which are the forget  $f_k$ , the input  $i_k$ , and the output  $o_k$  gates.

The forget gate  $f_k$  determines which information from the current input  $x_k$  and hidden state  $h_{k-1}$  of the previous LSTM cell should be stored or discarded through the sigmoid layer by directing each input information to either 1 or 0. The information directed at 1 is stored, while the information directed at 0 is discarded. The mathematical expression for the forget gate is presented in Eq. (1).

$$f_k = \sigma_s \bullet (w_f \bullet [h_{k-1}, x_k] + b_f) \quad (1)$$

The input gate  $i_k$  (cell status update) decides which new information needs to be stored in the memory cell. It receives the information from the current input data  $x_k$  and the previous hidden state  $h_{k-1}$  by passing them through the sigmoid and tanh layers to decide the information that needs to be either stored or discarded in the cell state. The mathematical expressions for these two layers are presented in Eq. (2).

$$\begin{cases} i_k = \sigma_s \bullet (w_i \bullet [h_{k-1}, x_k] + b_i) \\ \bar{C}_k = \tanh \bullet (w_c \bullet [h_{k-1}, x_k] + b_c) \end{cases} \quad (2)$$

The output information of the forget gate  $f_k$  is multiplied with the previous cell state  $C_{k-1}$  information. Then, it is added to a point-wise multiplication of the input gate  $i_k$  and the cell state vector  $\bar{C}_k$  to establish an updated memory cell for a current cell state  $C_k$ , as presented in Eq. (3).

$$C_k = f_k \bullet C_{k-1} + i_k \bullet \bar{C}_k \quad (3)$$

The output gate  $o_k$  determines the information for the next hidden state  $h_{k+1}$  output based on the filtered information contained in the cell state  $C_k$ . The mathematical expression of the new output gate  $o_k$  and the current hidden state  $h_k$  is presented in Eq. (4).

$$\begin{cases} o_k = \sigma_s \bullet (w_o \bullet [h_{k-1}, x_k] + b_o) \\ h_k = o_k \bullet \tanh(C_k) \end{cases} \quad (4)$$

In Eqs. (1)–(4),  $x_k$  is the input information at the time step  $k$ .  $\sigma_s (\bullet)$  is the sigmoid layer, which determines the information to retain or discard by weighing it towards 1 or 0, respectively. The  $\tanh (\bullet)$  is the hyperbolic tangent function used to control between  $-1$  and  $1$  the information flowing through the model to avoid fading. Each gate in the model has a weight  $w_f$ ,  $w_i$ ,  $w_c$ , and  $w_o$ , and a bias vector  $b_f$ ,  $b_i$ ,  $b_c$ , and  $b_o$ , which corresponds to the forget gate, input gate, memory cell, and output gate, respectively. These correspond to the respective gates to enhance the flexibility of the model to adapt to the training dataset.

## **2.2. Training procedure and hyperparameter selection for the LSTM model**

Data-driven methods can self-learn the correlation between the SOC and the measured variables, such as current, voltage, and temperature, in contrast to model-based methods. The model-based methods depend on the precise formulation of battery models to estimate the SOC, which is highly computationally expensive and difficult to establish [32]. The SOC is estimated as a time-series problem based on the theoretical equation of the Ah integration method. However, because of the memory cell and gating mechanism, an LSTM model is an appropriate method to solve this problem. In this paper, the time-varying current, voltage, and temperature variables are selected as the inputs, which are directly monitored during the battery test under the respective operating temperatures and working conditions, and the output is the SOC.

Several hyperparameters concerning the LSTM model's overall architecture are determined. The input window size and mini-batch size are the initial hyperparameters. The estimated SOC should be more reliable and accurate, with less noise caused by other nonlinear effects. Therefore, the input window's size should be accurately determined. The size should, however, be assumed to have a reasonable value rather than a very high one to meet the need for real-time SOC estimation. In this paper, the window size and mini-batch are defined as 50 and 32, respectively. The number of hidden and dropout layers is the second set of hyperparameters. DL models are known to perform better than shallow models. However, one or two hidden layers are capable of estimating the SOC. As a function of the

dropout layer, overfitting is decreased, and the model's performance is enhanced. Therefore, one hidden layer and one dropout layer are selected to make the model lighter and have higher computational efficiency. The number of hidden units in an LSTM cell is another crucial factor. Finding the ideal value is complicated since it turns out to have different effects on the SOC. After testing various units, including 10, 20, 30, and 50, 30 units are used to lighten the LSTM model because changing them does not improve the performance significantly. For the epochs, a lower number produced more noisy results, and an increased number increased the computation cost with no significant improvement. Therefore, 300 epochs are selected after a gradual search for optimal performance.

Using the ADAM optimizer, the gradient ( $\beta_1$ ) and squared gradient ( $\beta_2$ ) decay rates are defined as 0.9 and 0.999, respectively, with a constant learning rate of 0.01 and a gradient threshold of 1. After adjusting the afore mentioned hyperparameters, a fully connected LSTM layer is established to produce just one output, the desired SOC estimation, which is applicable in real-time. Therefore, the established model can derive the temporal dependencies from past and future information by capturing the battery's temporal contexts in both backward and forward directions. The hyperparameters used to establish the LSTM model in this paper are summarized in Table 1.

**Table 1. Hyperparameters selection for the LSTM model.**

<b>Hyperparameter</b>	<b>Unit</b>
LSTM layers (TL)	2
Fully connected layer	1
Feedforwardnet	10
Epochs	300
Hidden units	30
Initial learning rate	0.01
Time sliding window	50
Stochastic optimizer	ADAM
Mini-batch size	32
Dropout layer	1
$\beta_1$ & $\beta_2$	0.9 & 0.999

For the gradient, which refers to the model's weights dropping as anticipated, the difference between the estimated and actual SOC during the forward pass must be represented appropriately by the loss

function of the LSTM model. In this paper, the RMSE is used as the loss function, as presented in Eq. (5).

$$\text{Lossfunction} = \sqrt{\frac{1}{N} \sum_{k=1}^N (y_k - \hat{y}_k)^2} \quad (5)$$

In Eq. (5), N is the length of the data sequence;  $y_k$  is the actual SOC value and  $\hat{y}_k$  is the estimated SOC value at time step k.

In this paper, the LSTM is constructed using MATLAB. Then, a stochastic gradient optimizer, ADAM, is used as a default training optimizer due to its computational efficiency and requires low memory. The ADAM optimizer updates the model's weights and biases based on the gradient of the loss function in the forward and backward passes until a convergence measure with minimal loss is achieved [62,63].

However, due to the high nonlinearities during the battery's operation as a result of the operating temperatures and complex working conditions, the SOC estimation accuracy of the LSTM model is not optimal. Therefore, the WFEKF method is proposed, which is presented in Section 2.3.

### **2.3. Working principle of the WFEKF optimization method**

The KF method obtains the optimal state estimation based on the state-space model established for the system. Several advanced models of the conventional KF, such as the EKF, UKF, PF, etc., methods, have been successfully applied in many fields. The EKF method applies partial derivatives and the first-order Taylor series expansion to the system's inputs and nonlinearities to estimate the SOC of lithium-ion batteries [64]. Even though it is an optimal regression data processing method compared to the conventional KF, the estimated SOC is highly affected by the system's nonlinearities and uncertainties [65].

In this paper, an adaptive weighing factor is applied to the Kalman gain to recursively optimize its accurate scaling during the posteriori state estimate. Then, a fading factor is introduced to correct the uncertainties in the update of the posteriori error covariance matrix for accurate estimation, as presented in Eq. (6).

$$\begin{aligned} \hat{x}_k^+ &= \hat{x}_k^- + K_k^\gamma * e_k \\ s^{-(N-k)} P_{k+1|k}^+ &= A_{k-1} (s^{-(N-k)} P_k^-) A_{k-1}^T + Q_{k-1} \Rightarrow P_{k+1|k}^+ \\ &= A_{k-1} (s P_k^-) A_{k-1}^T + Q_{k-1} \end{aligned} \quad (6)$$

In Eq. (6),  $\hat{x}_k^+$  and  $\hat{x}_k^-$  are the posteriori and priori state estimates, respectively.  $e_k$  is the innovation residual, which is the difference between the previous and current measurements.  $K_k$  is the Kalman gain, which is the adjustment weight used to update the measurements to enhance the contribution of the residual to the priori state estimate during the posteriori state estimate.  $\gamma$  is the adaptive weighing factor, which is tuned within  $2 \leq \gamma \leq 4$  to denoise the estimated SOC and enhance its adaptability to the actual SOC. The update of the posteriori error covariance matrix is also expanded by  $s$  times, indicating that the estimation ability is optimized. The fading factor  $s$  is optimally tuned within a range of  $0.80 < s \leq 1$ , to adaptively adjust the estimation based on the extent of model mismatch and the error fluctuations. N is the total filtering time domain, and k is the arbitrary time in the operating domain. Meanwhile, all the other working steps of the conventional EKF method remain the same.

The SOC is the ratio of the available capacity to the nominal capacity of the battery. It is mathematically expressed, as presented in Eq. (7).

$$\begin{cases} SOC_k = 1 - DOD_k = \frac{Q_k}{Q_n} \times 100\% \\ SOC_k = SOC_0 - \frac{\int_0^k \eta I_k dk}{Q_n} \end{cases} \quad (7)$$

In Eq. (7),  $SOC_k$  is the estimated SOC, and  $DOD_k$  is the depth of discharge at time step  $k$ , where Coulombic efficiency and self-discharge are neglected.  $Q_k$  is the remaining capacity measured at time step  $k$  and  $Q_n$  is the nominal capacity, which is the maximum possible charge that can be stored in a battery.  $SOC_0$  is the initial SOC value,  $\eta$  is the Coulombic efficiency defined as 1, and  $I_k$  is the working current at time step  $k$ .

## **2.4. Data description and pre-processing**

### **2.4.1. Data description**

Several approaches have been used to establish better NN models: First, the NN model input is pre-processed to extract the relevant “features” from the battery’s response data. For lead-acid-based batteries, the variation in the terminal voltage directly correlates with the battery’s SOC. As a result, input for model training often simply uses the current and voltage of the battery. For nickel-metal hydride and lithium-ion batteries, due to the short-term dynamics of the terminal voltage, other inputs such as temperature are required by including pre-processed voltage derivatives to extract the nonlinear features of the voltage [30,31].

In the paper, as a temperature-conditioned LSTM model, three models are established with different training temperature datasets (cold, normal, and hot) and the same hyperparameter selections. Meanwhile, the testing temperature dataset is changed based on the purpose of the study. The training and testing datasets for each operating temperature variation include the current, voltage, and temperature. The variables are obtained with a standard sampling interval of 0.1 s.

### **2.4.2. Data pre-processing**

Since data processing is significant for accurate training of the model, the corresponding current, voltage, and temperature [ $I_k, V_k, T_k$ ] variables measured at each time step are used as the input. In the training process, an attention mechanism is introduced into the LSTM model. It extracts the relevant features from the input datasets by attaching weights. It optimizes the LSTM model’s training process to adaptively select the relevant intrinsic features for faster training. The summarized mathematical expression of the attention mechanism is presented in Eq. (8).

$$\tilde{x}_k = (e_k^1 x_k^1, e_k^2 x_k^2, \dots, e_k^n x_k^n)^T \Rightarrow x_k = \sum_{k=1}^N \beta_k h_k \quad (8)$$

In Eq. (8),  $\tilde{x}_k$  is the attention-weighted input, and  $e_k^n$  is a certain attention weight assigned to each of the features to measure the significance of the  $N$ -dimensional feature at time step  $k$ .  $x_k$  is the context vector, which is a weighted sum of the attention probability ( $\beta_k$ ) and hidden state ( $h_k$ ) information at time step  $k$ .

## **2.5. Flowchart of the LSTM and LSTM-WFEKF models for SOC estimation**

The SOC estimated by the LSTM model with the current and temperature variables are taken as inputs into the WFEKF method to denoise and optimize based on the estimated inputs for the final SOC, as presented in the flowchart in Fig. 2.

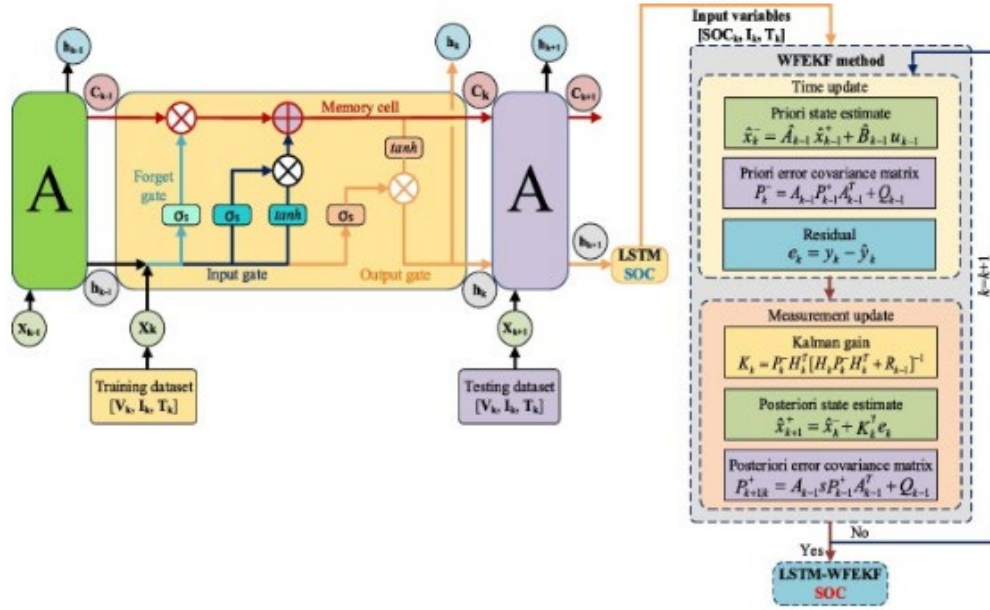


Fig.2. The flowchart of the LSTM and LSTM-WFEKF models for SOC estimation.

## 2.6. Performance evaluation metrics for the LSTM and LSTM-WFEKF models

In this paper, to critically evaluate the performance of the LSTM and LSTM-WFEKF models for SOC estimation at different temperatures and working conditions, the ME, MAE, RMSE, and  $R^2$  metrics are used. The mathematical expressions for the metrics are presented in Eq. (9).

$$\left\{ \begin{array}{l} E_k = y_k - \hat{y}_k \\ ME = \max_{1, 2, \dots, N} |E_k| \\ MAE = \frac{1}{N} \sum_{k=1}^N |y_k - \hat{y}_k| \\ RMSE = \sqrt{\frac{1}{N} \sum_{k=1}^N (y_k - \hat{y}_k)^2} \\ R^2 = 1 - \frac{\sum_{k=1}^N (y_k - \hat{y}_k)^2}{\sum_{k=1}^N (y_k - \bar{y})^2} \end{array} \right. \quad (9)$$

In Eq. (9),  $k$  is the non-missing data steps,  $N$  is the total number of data sample steps, and  $E_k$  is the estimated SOC error, which is the difference between the actual SOC value ( $y_k$ ) and the estimated SOC ( $\hat{y}_k$ ) at time step  $k$ .  $\bar{y}$  is the average value of the actual SOC at time step  $k$ . ME is the absolute maximum error value in the estimated error data sequence. The MAE means that all the individual differences (both positive and negative values) are equally weighted in the error data sequence. The RMSE measures how dispersed the error is from the actual SOC values. The  $R^2$  (coefficient of determination) measures the perfection of the models in estimating the SOC compared to the actual SOC values.

## 3. Experimental analysis

### 3.1. Experimental test platform and procedure

An LNCM70Ah (lithium nickel manganese cobalt oxide) lithium-ion battery is used for the experiments under varying operating temperatures. It has a nominal capacity and voltage of 70 Ah and 3.7 V,

respectively. It has a cathode electrode made of nickel cobalt manganese and an anode electrode made of natural graphitic carbon with a metallic backing. The basic technical specifications of the LNCM70Ah battery are presented in Table 2.

Table 2. Basic technical specifications of the lithium-ion battery.

Parameter	Value	Parameter	Value
Nominal capacity	70 Ah	Standard discharge current	3 C
Nominal voltage	3.7 V	Maximum discharge current	5 C
Charge cut-off voltage	4.2 V	Internal resistance (Impedance)	0.5–1 mΩ
Discharge cut-off voltage	2.75 V	Discharge temperatures	–20–60 °C
Maximum charge current	1C	Dimension: l × w × h	148 × 27 × 96 (mm)

A high precision and multi-range Neware battery test equipment (CT-4016-5V100A-NTFA) is used for the experimental tests. It has a maximum current of 100 A, a range of charge and discharge voltage of 25~100 V, and a maximum charge and discharge power of 12 kW. The temperature testing equipment is a DGBELL BTT-331C, which controls the operating temperature of the battery under cold (– 10 °C), normal (25 °C), and hot (50 °C) for each working condition test. The experimental test platform for the temperature variation and the working condition tests is presented in Fig. 3.

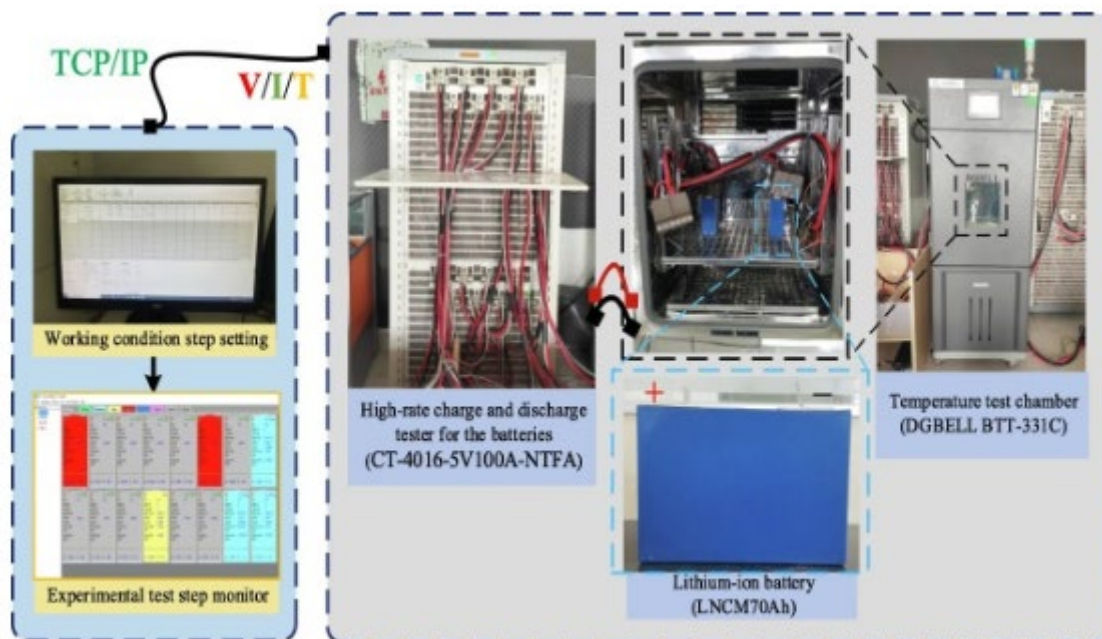


Fig.3. Experimental test platform constructed for the temperature tests.

Fig. 3 shows the experimental testing platform set-up to obtain the charge–discharge characteristic responses of the lithium-ion battery, such as the current and terminal voltage, for all temperature variations and working conditions. The main components of the experimental platform are the battery test equipment (charge–discharge control circuit, a circuit measurement system, a signal detector, and electronic load), temperature test equipment, and a direct current power supply cable connected to the lithium-ion battery. A general-purpose computer is used for setting, monitoring, and retrieving the response data at the end of the test. The experimental results of the cyclic charge and discharge states are visually recorded, displayed, and retrieved from the general-purpose computer, which mainly includes the time-varying current, voltage, temperature, capacity, energy, power, etc., values of the lithium-ion battery. From the capacity tests, the maximum available capacities of the battery are 40, 70, and 52 Ah at – 10, 25, and 50 °C operating temperatures, respectively.

### **3.2. Test procedures of the BBDST, HPPC, and DST working conditions**

#### **3.2.1. BBDST working condition**

The experimental data for the BBDST working condition is obtained by processing the data retrieved from the start, acceleration, slide, brake, rapid acceleration, and stop of the Beijing bus. A constant current-constant voltage (CC-CV) is applied until the maximum charge voltage is reached, and a 30-minute rest is followed by the complex working steps, as presented in Table 3.

Table 3. The complex working steps of the Beijing bus.

Step	$P_c$ (W)	Step time (s)	Total time (s)	Working status
1	75	21	21	Start
2	145	12	33	Acceleration
3	9	16	49	Slide
4	-30	6	55	Brake
5	75	21	76	Acceleration
6	9	16	92	Slide
7	-30	6	98	Brake
8	145	9	107	Acceleration
9	185	6	113	Rapid acceleration
10	75	21	134	Acceleration
11	9	16	150	Slide
12	-30	6	156	Brake
13	145	9	165	Acceleration
14	185	6	171	Rapid acceleration
15	75	21	192	Acceleration
16	9	16	208	Slide
17	-70	9	217	Brake
18	-30	6	229	Brake
19	9	71	300	Stop

Assuming the charging to be negative and the discharging to be positive, the characteristics of the current and voltage datasets under the BBDST working condition for each temperature variation are presented in Fig. 4.

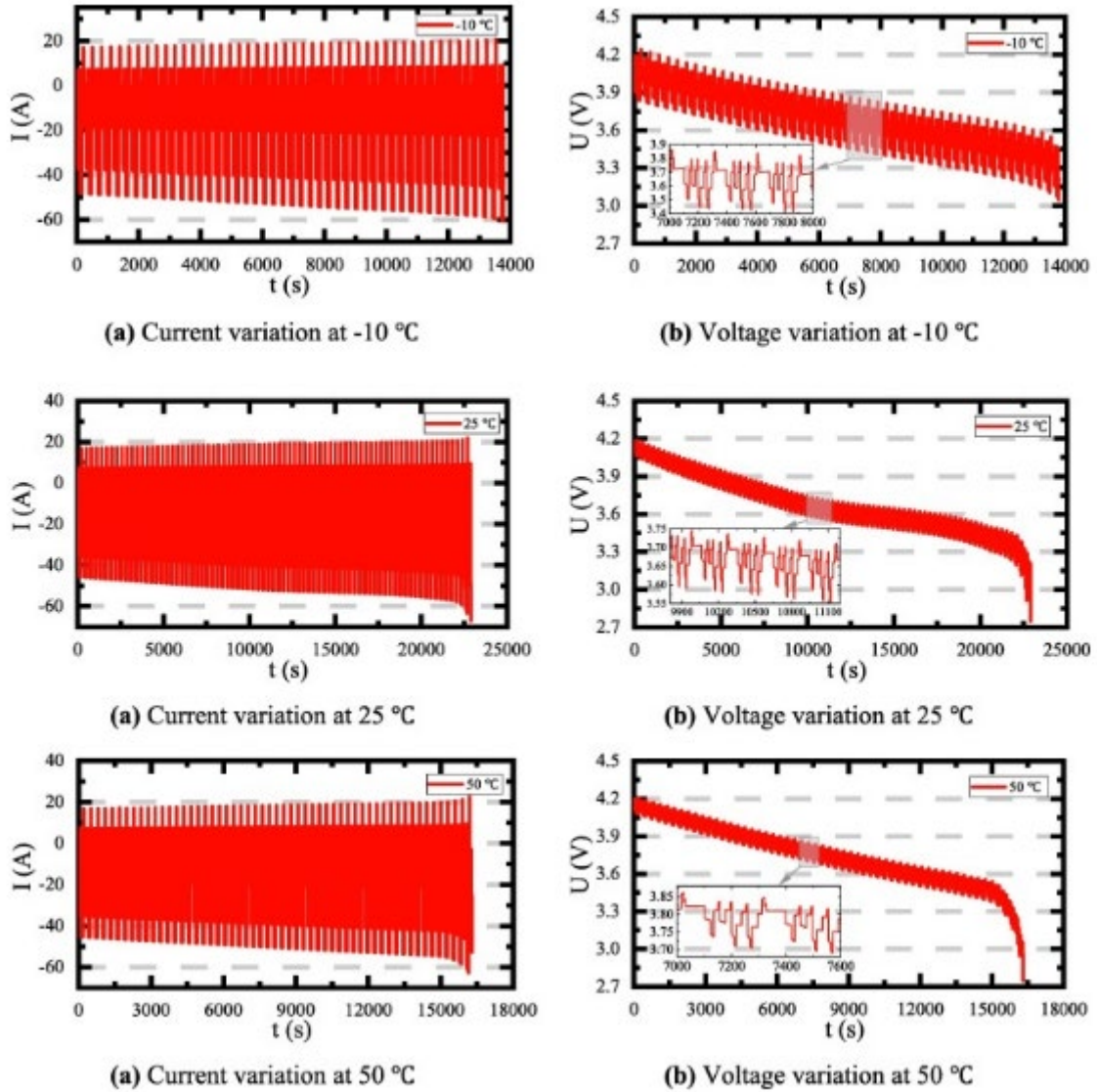


Fig. 4. The characteristics of the current and voltage datasets under the BBDST working condition.

### 3.2.2. HPPC working condition

The HPPC test measures the pulse capability of the lithium-ion battery under varying step discharge levels at different time intervals. The experimental steps are illustrated as follows:

- (i) A CC-CV is applied to charge the battery to its maximum charge voltage.
- (ii) The battery is rested for 40 min to ensure electrochemical and thermal equilibrium before the next test profile.
- (iii) A 10-second discharge pulse is applied at a constant current rate depending on the operating temperature and the maximum available capacity of the battery. The battery is then rested for 40 s.
- (iv) A 10-second charge pulse is initiated at a 1C current rate, followed by a rest time of 2 min at the same current rate based on the operating temperature.
- (v) A discharge pulse at a current rate of 6 min is applied to end the first cycle.
- (vi) The next cyclic HPPC test is conducted on the battery by repeating Steps (ii) to (v) for the ten (10) SOC levels at a 10% discharge interval.

The corresponding open-circuit voltage for each SOC level is accurately measured before the start of the next HPPC test cycle.

Assuming the charging is negative and the discharging is positive, the characteristics of the current and voltage datasets under the HPPC working condition for each temperature variation used for the SOC estimation are presented in Fig. 5.

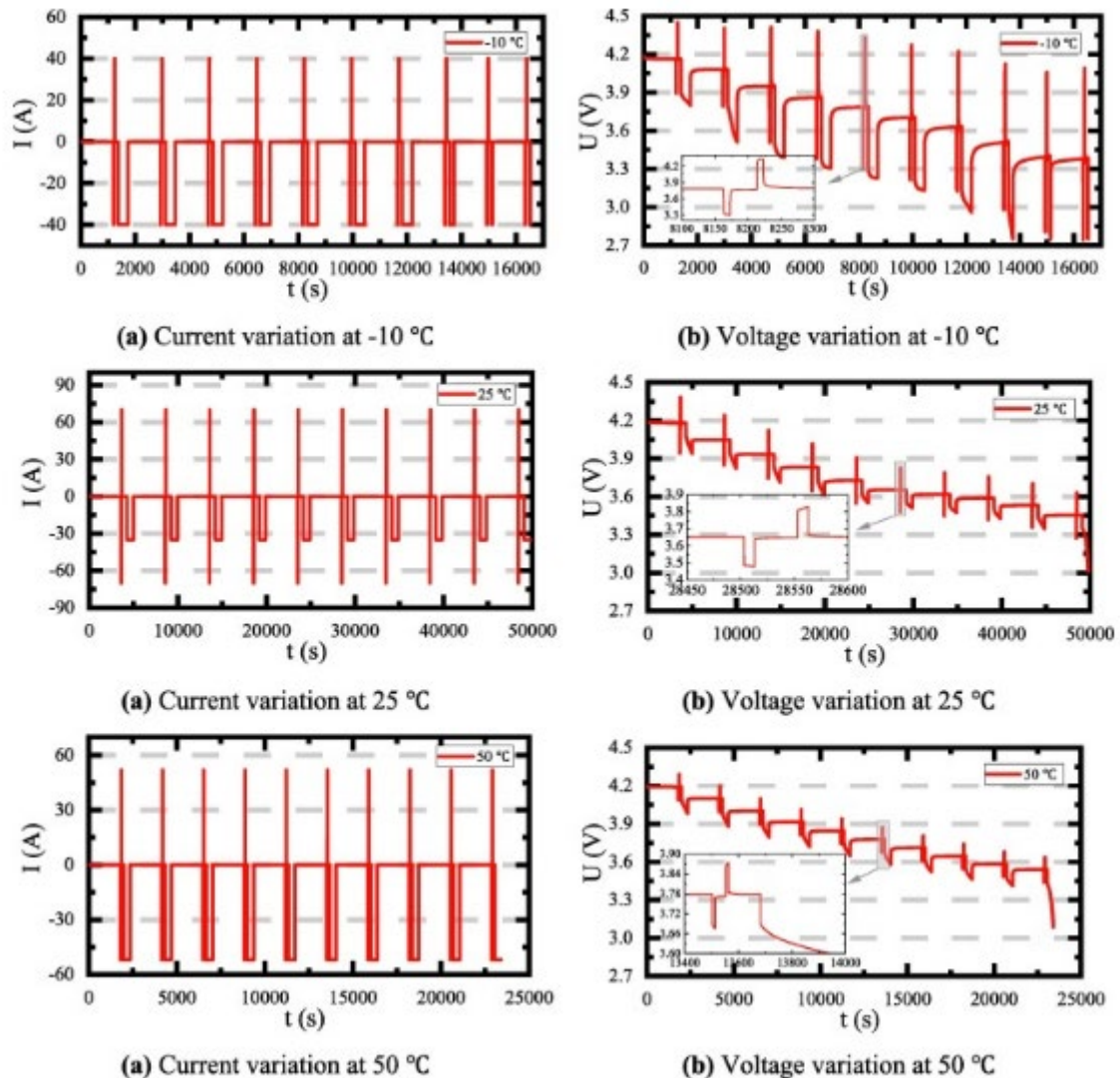


Fig.5. The characteristics of the current and voltage datasets under the HPPC working condition.

### **3.2.3. DST working condition**

The complex DST working condition is self-defined. The experimental test steps are described as follows:

- (i) The battery is charged to a maximum charge voltage of 4.20 V with a CC-CV. Then, a rest time of 30 min to ensure thermal and electrochemical equilibrium before the next test profile.
  - (ii) A CC discharge is applied at a rate of 0.5C for 4 min, which is dependent on the defined operating temperature. Then, the battery is rested for 30 s after the discharge.
  - (iii) The battery is charged at a CC rate of 0.5C for 2 min and rested for 30 s.
  - (iv) A CC discharge is applied at a rate of 1C for 4 min.
- Steps (iii) and (iv) are repeated until a cut-off voltage is reached.

Assuming the charging is negative and the discharging is positive, the characteristics of the current and voltage datasets under the DST working condition for each temperature variation used for the SOC estimation are presented in Fig. 6.

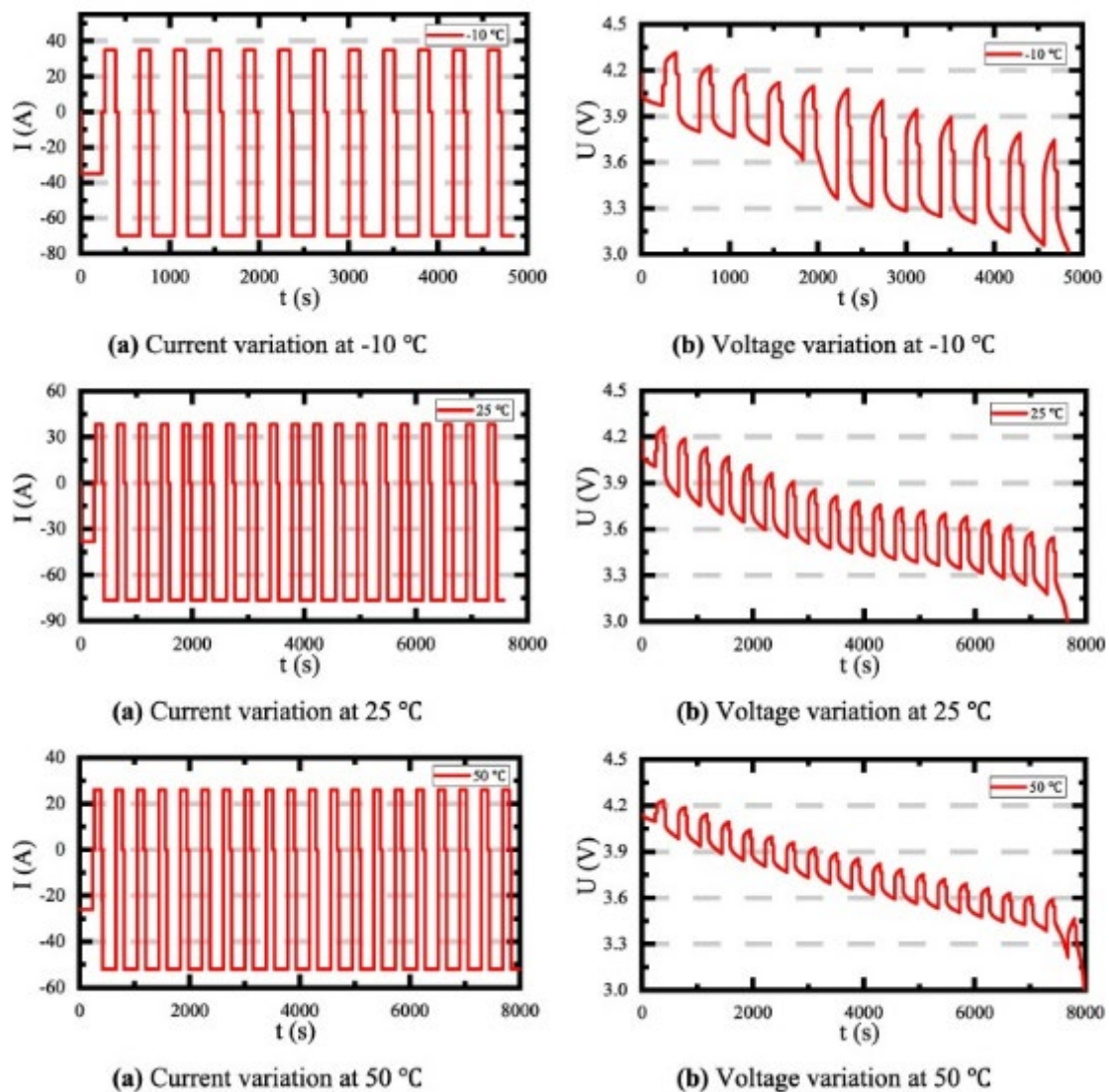


Fig. 6. The characteristics of the current and voltage datasets under the DST working condition.

### 3.3. SOC estimation and performance evaluation of the LSTM and LSTMWFEKF models

In this paper, a computer system with an AMD Ryzen 5 2600 Six-Core processor @ 2.60 GHz, 16 GB of memory, and a 64-bit OS (x64-based processor) is used for the training and testing of the LSTM model for SOC estimation. An epoch of 300 is selected after conducting an optimal search criterion to avoid overfitting in the global optimization process. To examine the generalization and TL abilities of the LSTM model, the training and testing sequence for SOC estimation is presented in Table 4.

Table 4. The sequence for the training and testing of the LSTM model.

Working conditions		Temperatures		
Training	Testing	-10 °C	25 °C	50 °C
BBDST	HPPC	-10/25/50 °C	-10/25/50 °C	-10/25/50 °C
BBDST	DST	-10/25/50 °C	-10/25/50 °C	-10/25/50 °C
DST	BBDST	-10/25/50 °C	-10/25/50 °C	-10/25/50 °C

The validation and training states to initialize the training of the LSTM model and its training progress RMSE and loss curves are presented in Fig. 7.

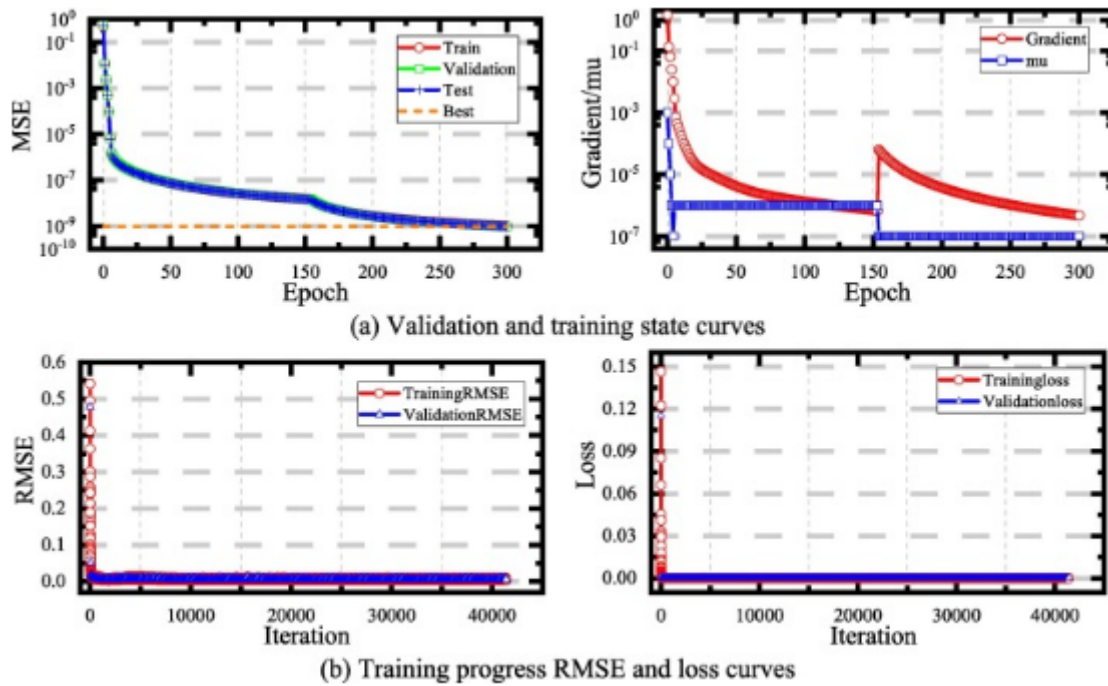
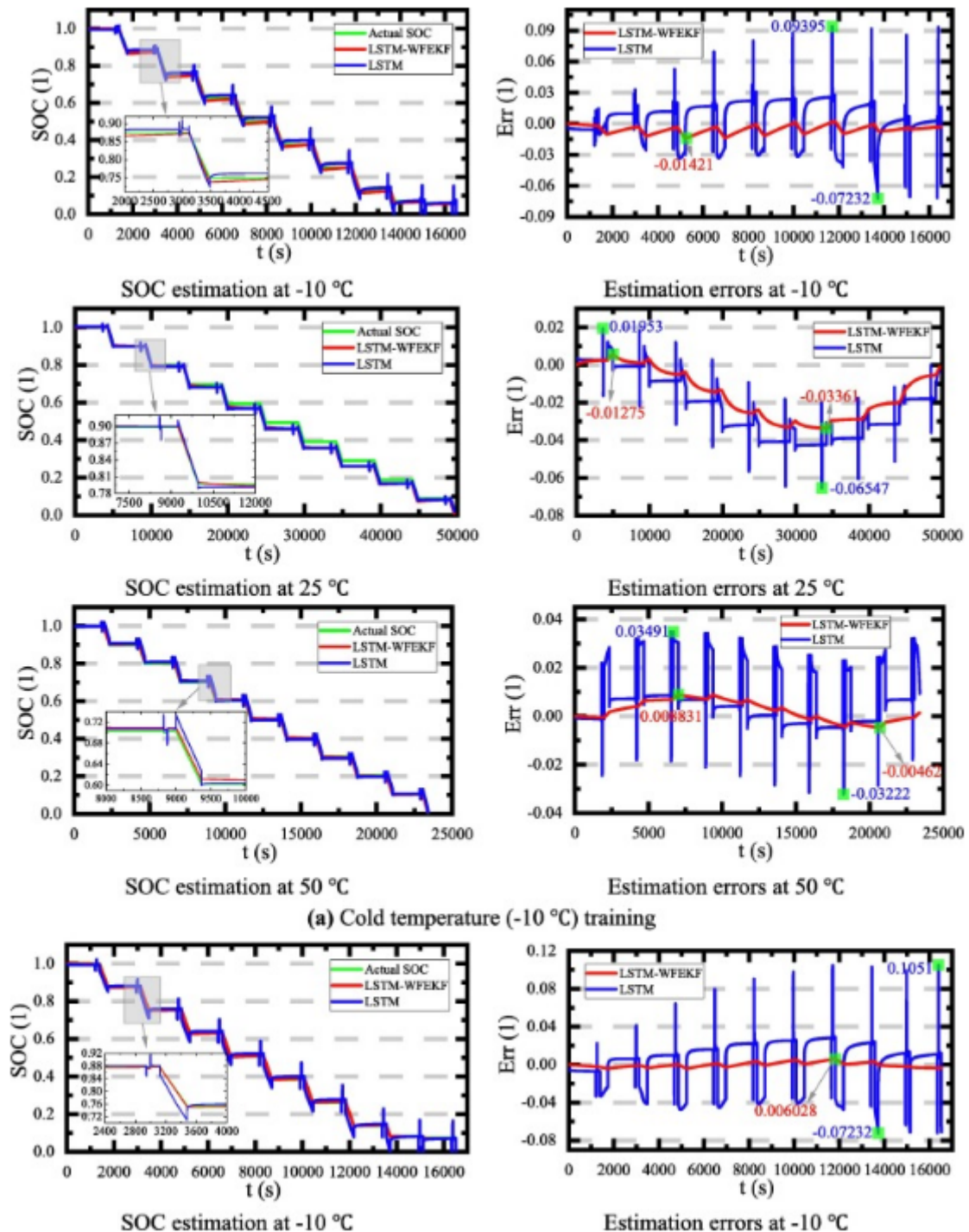


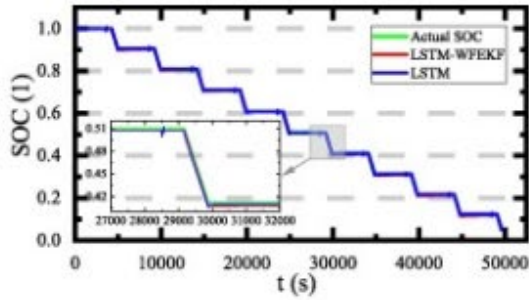
Fig.7. Validation and training progress of the LSTM model.

The validation and training state performance curves of the parallel training pool are presented in Fig. 7 (a), which shows the maximum gradient and the mu values with the total number of epoch iterations to initialize the training of the LSTM model. Fig. 7 (b) shows the curves for the training progress, the trained model's RMSE and loss versus total iterations during the training of the LSTM model.

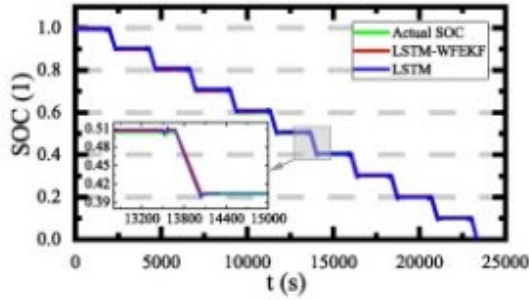
### 3.3.1. SOC estimation using the LSTM and LSTM-WFEKF models

Based on the training and testing temperature sequence presented in Table 4, the SOC estimation results for the LSTM and LSTM-WFEKF models under the HPPC working condition are presented in Fig. 8.



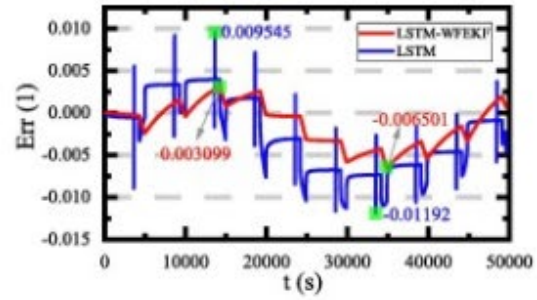


SOC estimation at 25 °C

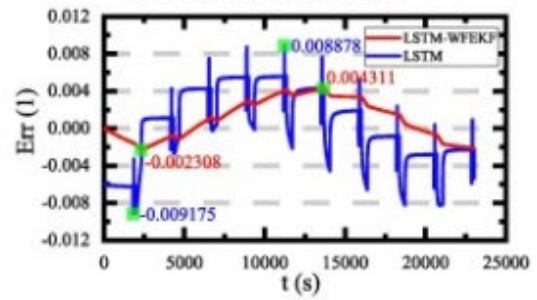


SOC estimation at 50 °C

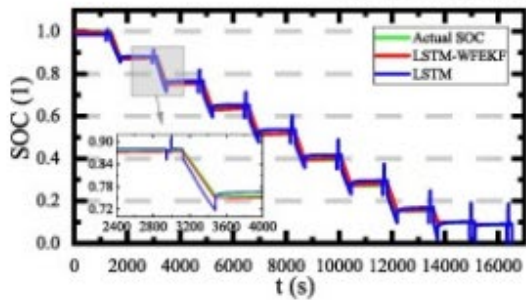
(b) Normal temperature (25 °C) training



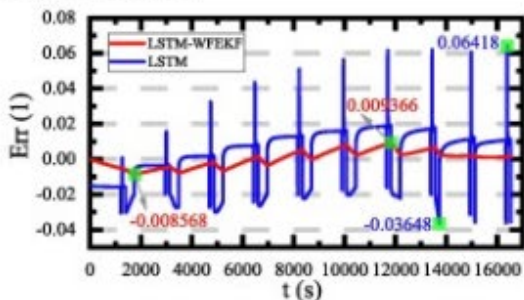
Estimation errors at 25 °C



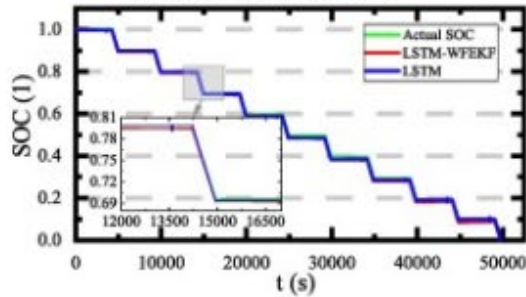
Estimation errors at 50 °C



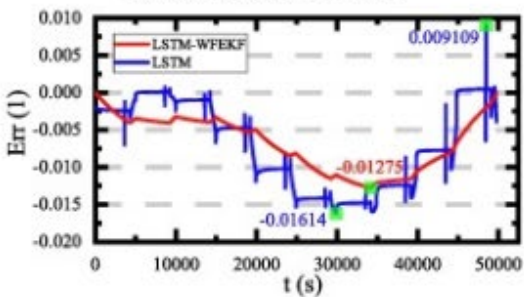
SOC estimation at -10 °C



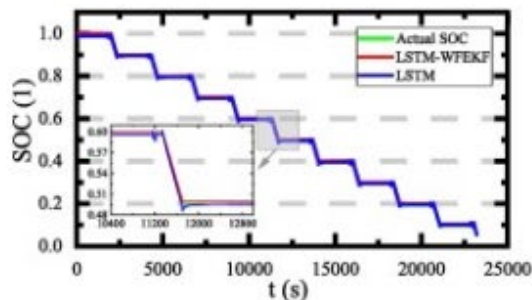
Estimation errors at -10 °C



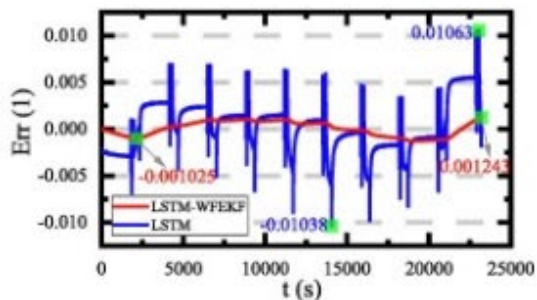
SOC estimation at 25 °C



Estimation errors at 25 °C



SOC estimation at 50 °C



Estimation errors at 50 °C

(c) Hot temperature (50 °C) training

Fig. 8. SOC estimation results of the LSTM and LSTM-WFEKF models at different temperatures under the HPPC working condition.

To study the effects of different operating temperatures on the SOC, the LSTM model is tested using different temperature datasets under the HPPC working condition. Then, the WFEKF method is proposed to denoise and further optimize the final SOC.

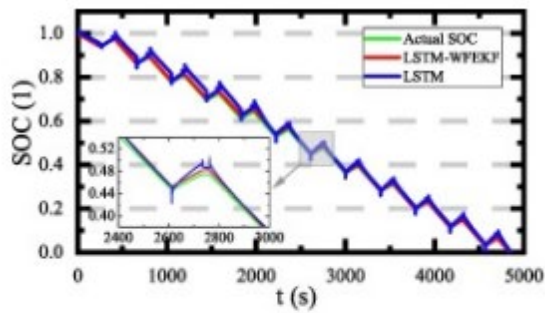
In Fig. 8 (a), it can be observed that training the LSTM model with a  $-10\text{ }^{\circ}\text{C}$  (cold) dataset introduces more noise to the system, which increases the “spikes” in the estimation caused by the increased resistance and self-discharge at cold temperatures. It can be observed that the noise increases with the decreasing SOC level. It results in high SOC estimation ME values of 9.395% and 6.547% when the  $-10$  and  $25\text{ }^{\circ}\text{C}$  testing datasets are used, respectively. However, it can be observed that the noise in the estimated SOC error is overcome when a  $50\text{ }^{\circ}\text{C}$  testing dataset is used, which results in an ME value of 3.491%. Meanwhile, the proposed LSTM-WFEKF model does well in denoising and optimizing the final SOC to result in estimated ME values of 1.421%, 3.361%, and 0.8831% using testing temperature datasets of  $-10$ ,  $25$ , and  $50\text{ }^{\circ}\text{C}$ , respectively.

In Fig. 8 (b), it can also be observed that training the LSTM model with a  $25\text{ }^{\circ}\text{C}$  (normal) dataset shows the least noise effect for the  $25$  and  $50\text{ }^{\circ}\text{C}$  tests by estimating the SOC with ME values of 1.192% and 0.9175%, respectively. However, testing with the  $-10\text{ }^{\circ}\text{C}$  dataset shows a high ME value of 10.51%, which means the noise is inherent in the  $-10\text{ }^{\circ}\text{C}$  dataset. This is a result of the increased resistance and self-discharge at cold operating temperatures. Meanwhile, the proposed LSTM-WFEKF model denoises and optimizes the final SOC to result in estimated ME values of 0.6028%, 0.6501%, and 0.4311% using testing temperatures of  $-10$ ,  $25$ , and  $50\text{ }^{\circ}\text{C}$ , respectively.

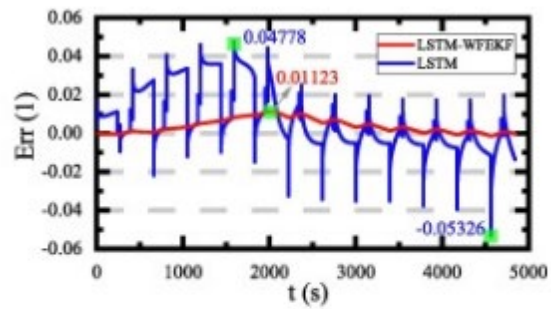
In Fig. 8 (c), it can be observed that training with a  $50\text{ }^{\circ}\text{C}$  dataset offers the best choice to ensure minimized estimation errors and noise for the three testing temperature datasets. The ME values of the LSTM model are 6.418%, 1.614%, and 1.063% using the testing datasets at  $-10$ ,  $25$ , and  $50\text{ }^{\circ}\text{C}$ , respectively, which also indicates that the  $-10\text{ }^{\circ}\text{C}$  testing dataset has the highest ME. While using testing temperatures of  $-10$ ,  $25$ , and  $50\text{ }^{\circ}\text{C}$ , the proposed LSTM-WFEKF model yields estimated ME values of 0.9366%, 1.275%, and 0.1243%, respectively.

Generally, these results show that using the  $50\text{ }^{\circ}\text{C}$  datasets for training the LSTM model ensures a less noisy and more accurate SOC estimation at varying testing temperatures compared to other training datasets under the HPPC working condition.

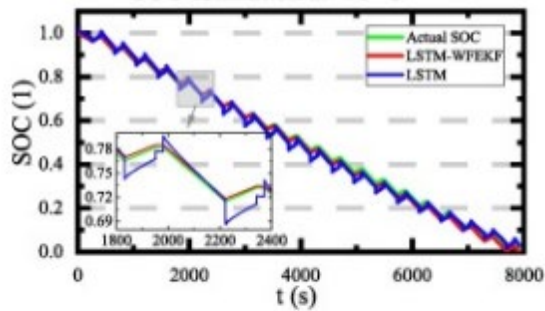
The SOC estimation results for the LSTM and LSTM-WFEKF models at a training temperature variation of  $-10$ ,  $25$ , and  $50\text{ }^{\circ}\text{C}$  under the DST working condition are conducted and presented in Fig. 9.



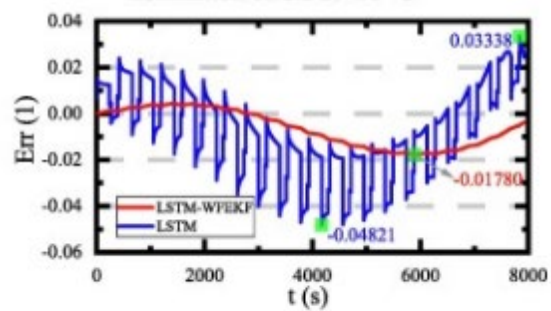
SOC estimation at -10 °C



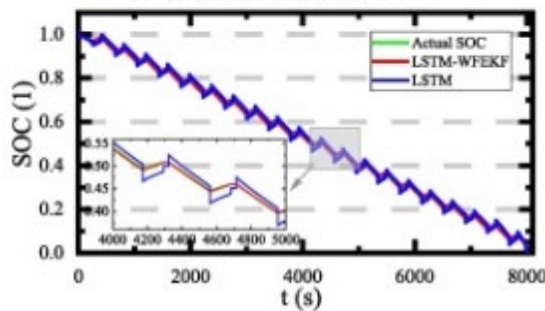
Estimation errors at -10 °C



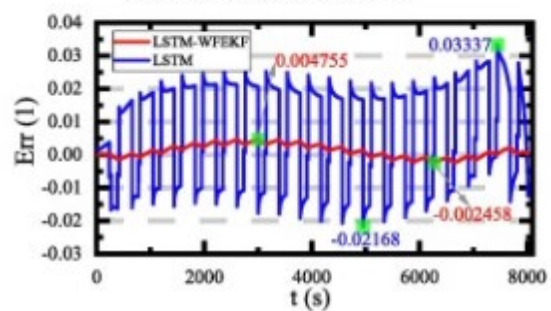
SOC estimation at 25 °C



Estimation errors at 25 °C

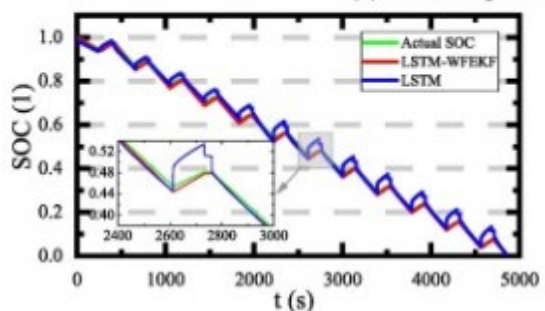


SOC estimation at 50 °C

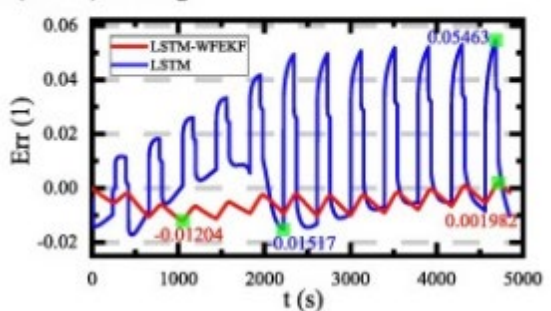


Estimation errors at 50 °C

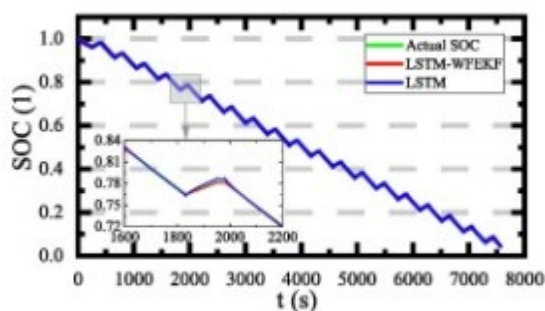
(a) Cold temperature (-10 °C) training



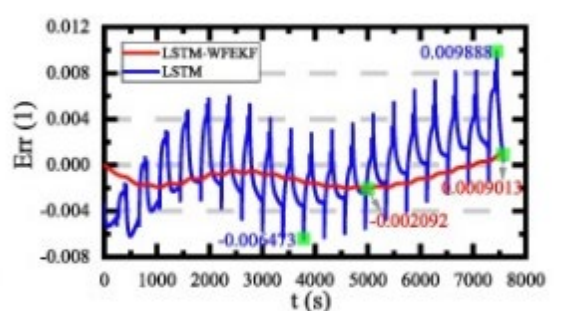
SOC estimation at -10 °C



Estimation errors at -10 °C



SOC estimation at 25 °C



Estimation errors at 25 °C

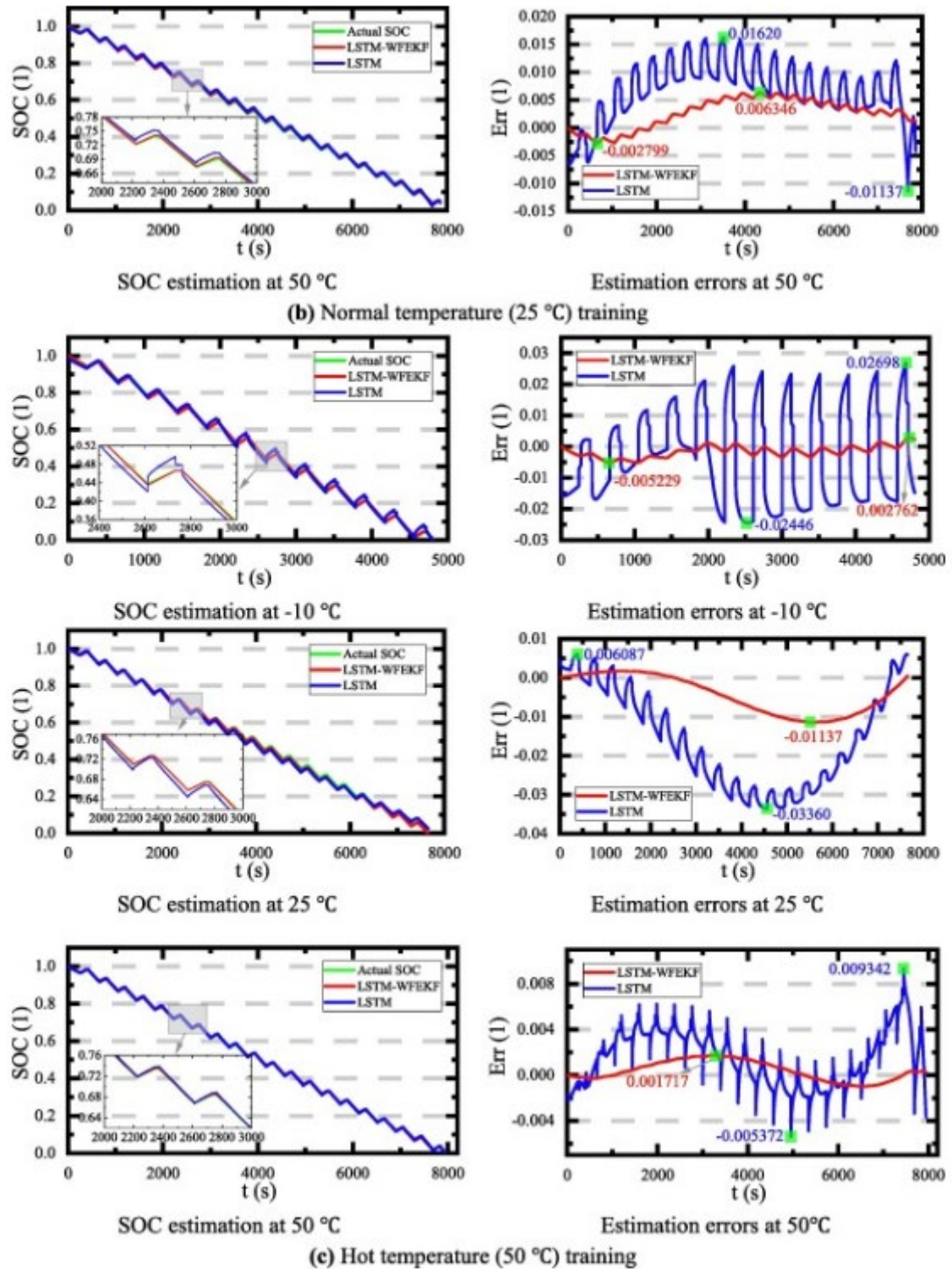


Fig. 9. SOC estimation results of the LSTM and LSTM-WFEKF models at different temperatures under the DST working condition.

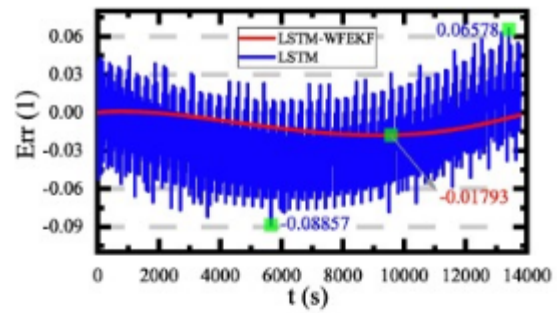
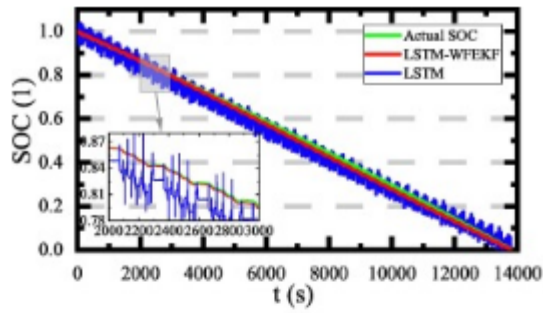
In Fig. 9 (a), it can be observed that training the LSTM model under the DST working condition with a  $-10\text{ }^{\circ}\text{C}$  (cold) dataset introduces noise to the estimation. It causes the estimation to have large error spikes and variations around the actual SOC, resulting in high ME values of 5.326% and 4.821% when tested with  $-10$  and  $25\text{ }^{\circ}\text{C}$  datasets, respectively. However, it can be observed that the noise in the training dataset is reduced when a  $50\text{ }^{\circ}\text{C}$  testing dataset is used for the estimation, which results in an

ME value of 3.337%. Moreover, employing testing temperatures of  $-10$ ,  $25$ , and  $50$  °C datasets, the proposed LSTM-WFEKF model performs well enough in denoising and optimizing the final SOC, with estimated ME values of 1.123%, 1.780%, and 0.4755%, respectively. Furthermore, it can be observed that a similar pattern of estimation errors under the HPPC working condition occurs under the DST working condition when the  $-10$  °C dataset is used in training the LSTM model.

In Fig. 9 (b), it can also be observed that training the LSTM model with a  $25$  °C (normal) dataset shows a minimal noise effect for the  $25$  and  $50$  °C tests, estimating ME values of 0.9888% and 1.620%, Fig. 8. SOC estimation results of the LSTM and LSTM-WFEKF models at different temperatures under the HPPC working condition. 12 respectively. However, testing with the  $-10$  °C dataset yields a high ME of 5.463%, confirming that the  $-10$  °C testing dataset has inherent noise. Meanwhile, employing testing temperatures of  $-10$ ,  $25$ , and  $50$  °C, the proposed LSTM-WFEKF model denoises and optimizes the final SOC, resulting in ME values of 1.204%, 0.2092%, and 0.6346%, respectively.

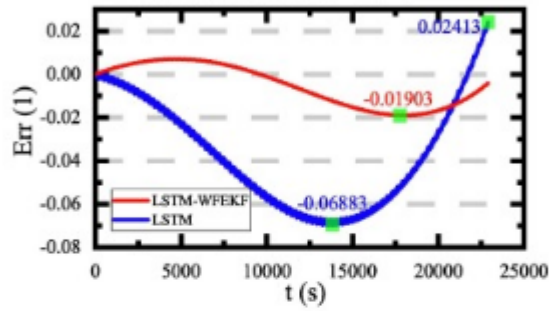
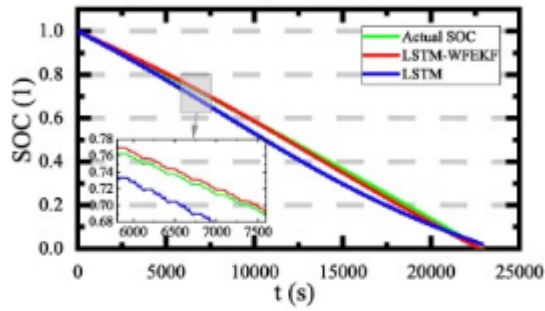
As presented in Fig. 9 (c), training the LSTM model with a  $50$  °C (hot) dataset is the optimal choice for ensuring minimal errors and noise Fig. 8. (continued). 13 effects for three testing temperatures under the DST working condition. Using testing temperatures of  $-10$ ,  $25$ , and  $50$  °C, the ME values are 2.698%, 3.360%, and 0.9342%, respectively. Furthermore, employing testing temperatures of  $-10$ ,  $25$ , and  $50$  °C, the proposed LSTM-WFEKF model yields SOC estimation ME values of 0.5229%, 1.1137%, and 0.1717%, respectively.

For further verification, the SOC estimation is conducted for the LSTM and LSTM-WFEKF models under the BBDST working condition using training temperatures of  $-10$ ,  $25$ , and  $50$  °C from the DST working condition experiment, as presented in Fig. 10.



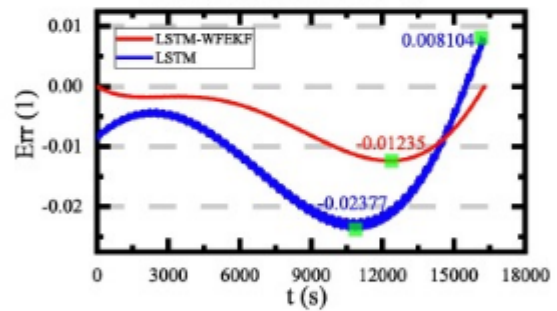
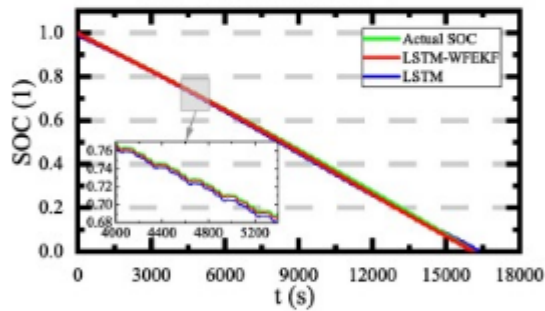
SOC estimation at -10 °C

Estimation errors at -10 °C



SOC estimation at 25 °C

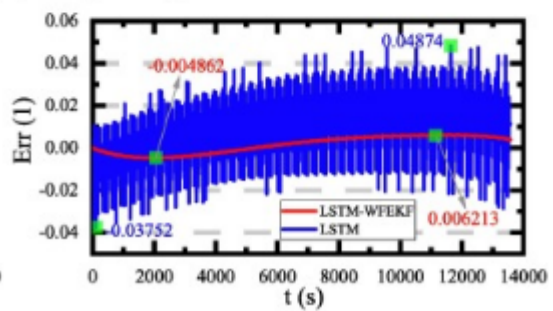
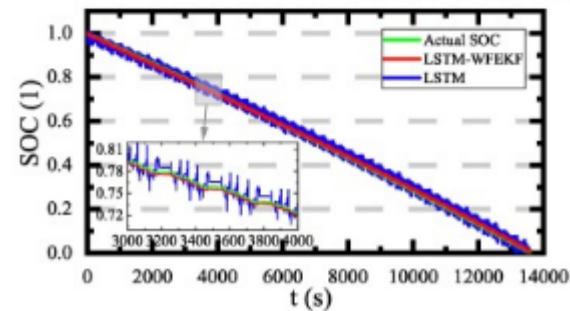
Estimation errors at 25 °C



SOC estimation at 50 °C

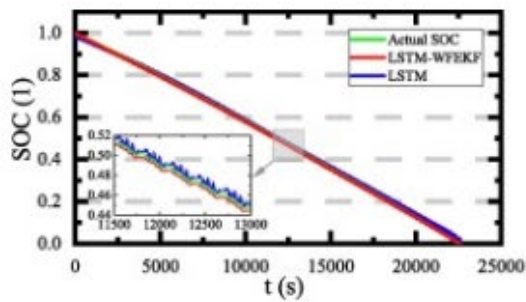
Estimation errors at 50 °C

(a) Cold temperature (-10 °C) training

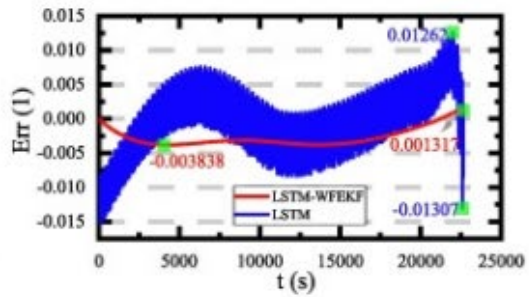


SOC estimation at -10 °C

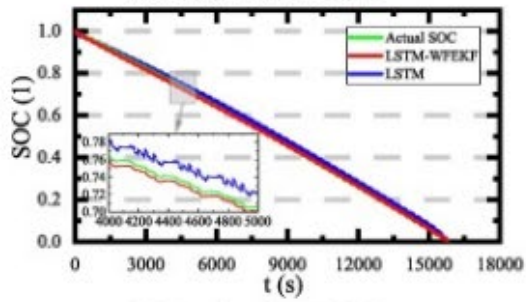
Estimation errors at -10 °C



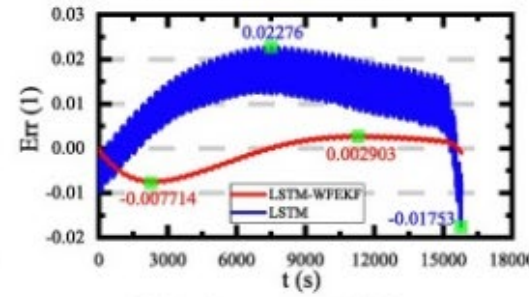
SOC estimation at 25 °C



Estimation errors at 25 °C

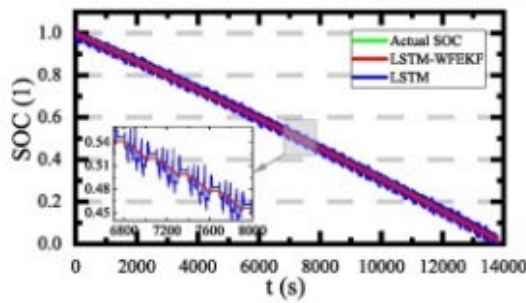


SOC estimation at 50 °C

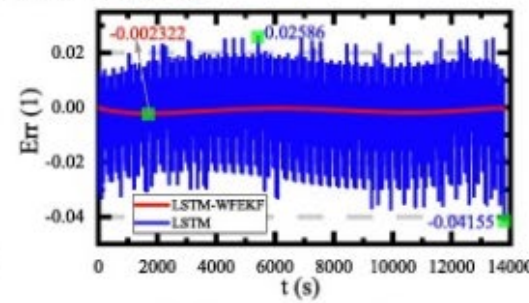


Estimation errors at 50 °C

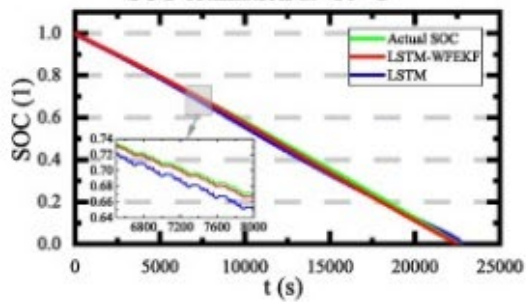
(b) Normal temperature (25 °C) training



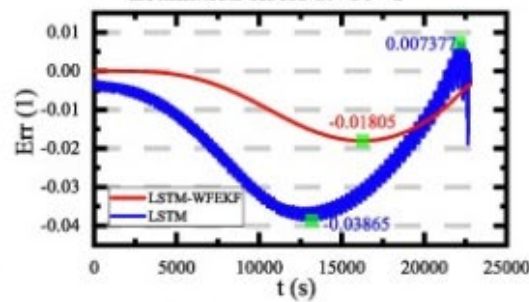
SOC estimation at -10 °C



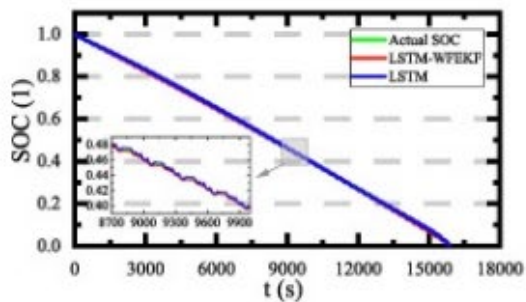
Estimation errors at -10 °C



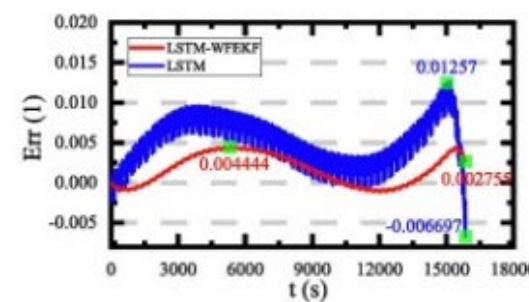
SOC estimation at 25 °C



Estimation errors at 25 °C



SOC estimation at 50 °C



Estimation errors at 50 °C

(c) Hot temperature (50 °C) training

Fig. 10. SOC estimation results of the LSTM and LSTM-WFEKF models at different temperatures under the BBDST working condition.

In Fig. 10 (a), it can be observed that training the LSTM model with a  $-10\text{ }^{\circ}\text{C}$  (cold) dataset under the BBDST working condition results in noisy and unstable SOC estimation. It results in large U-shaped error curves and variations from the actual SOC, leading to high ME values of 8.857% and 6.883% when tested with  $-10$  and  $25\text{ }^{\circ}\text{C}$  datasets, respectively. In particular, for the cold-to-cold temperature training and testing, high noise effects are observed, which also verifies that they are unsuitable matching pairs for the model. However, it can be observed that the error reduces significantly when a  $50\text{ }^{\circ}\text{C}$  dataset is used for testing or estimation, which results in an ME value of 2.377%. Furthermore, using testing temperature datasets of  $-10$ ,  $25$ , and  $50\text{ }^{\circ}\text{C}$ , the proposed LSTM-WFEKF model performs well in denoising and optimizing the final SOC, with estimated ME values of 1.793%, 1.903%, and 1.235%, respectively. Under the BBDST working condition, when the LSTM model is trained with a  $-10\text{ }^{\circ}\text{C}$  dataset, similar estimation error effects are also observed as exhibited under the HPPC and DST working conditions.

Also, as presented in Fig. 10 (b), comparably, training the LSTM model with a  $25\text{ }^{\circ}\text{C}$  (normal) dataset has moderate noise effects for the  $25$  and  $50\text{ }^{\circ}\text{C}$  tests, estimating the SOC with ME values of 1.307% and 2.276%, respectively. However, testing with the  $-10\text{ }^{\circ}\text{C}$  dataset yields a high ME value of 4.874%, reiterating the inherent noise effect in the  $-10\text{ }^{\circ}\text{C}$  testing dataset. For the  $-10$ ,  $25$ , and  $50\text{ }^{\circ}\text{C}$  tests under the BBDST working condition, similar estimation error effects are observed for both the HPPC and DST working conditions. Meanwhile, the proposed LSTMWFEKF model denoises and optimizes the final SOC using testing temperatures of  $-10$ ,  $25$ , and  $50\text{ }^{\circ}\text{C}$ , yielding ME values of 0.6213%, 0.3838%, and 0.7714%, respectively.

Furthermore, in Fig. 10 (c), the results show that training the LSTM model with a  $50\text{ }^{\circ}\text{C}$  (hot) dataset is the right approach for ensuring estimations with reduced noise and ME values for the three testing temperatures under this working condition. The ME values are 4.155%, 3.865%, and 1.257% using testing temperatures of  $-10$ ,  $25$ , and  $50\text{ }^{\circ}\text{C}$ , respectively. However, when tested at  $-10$ ,  $25$ , and  $50\text{ }^{\circ}\text{C}$ , the proposed LSTM-WFEKF model delivers SOC estimation ME values of 0.2322%, 1.805%, and 0.4444%, respectively.

Generally, the estimation results under the BBDST working condition also confirm the findings under the HPPC and DST working conditions that using the  $50\text{ }^{\circ}\text{C}$  datasets for the training ensures less noisy estimates and good SOC ME values at different temperatures than the other temperatures. It can also be observed that whenever a  $25\text{ }^{\circ}\text{C}$  testing dataset is trained under different temperatures ( $-10$  and  $50\text{ }^{\circ}\text{C}$ ), it results in a U-shaped error profile (error initializes appreciably well but diverges in the middle of the estimation and converges towards the end of the estimation). Similarly, this is also observed under the HPPC and DST working conditions, which confirms the U-shaped error profile and provides a signal that it is not advisable to test a normal ( $25\text{ }^{\circ}\text{C}$ ) temperature with neither cold nor hot temperature datasets.

Even though under the HPPC, DST, and BBDST working conditions, the LSTM model is highly affected by the high-level battery discharge, which results in high errors. In addition to the denoising and optimization by the LSTM-WFEKF model, it does well in correcting these end-of-discharge errors to give accurate estimates.

Furthermore, it can be observed that the tested SOC estimation results under the HPPC, DST, and BBDST working conditions are consistent for each training and testing temperature sequence, respectively, using the LSTM model, which verifies the findings in this paper.

### 3.3.2. Performance evaluation of the LSTM and LSTM-WFEKF models

The critical performance evaluations of the LSTM and LSTM-WFEKF models for SOC estimation under the HPPC working condition are conducted using the MAE, RMSE, and R2 metrics, as presented in Fig. 11.

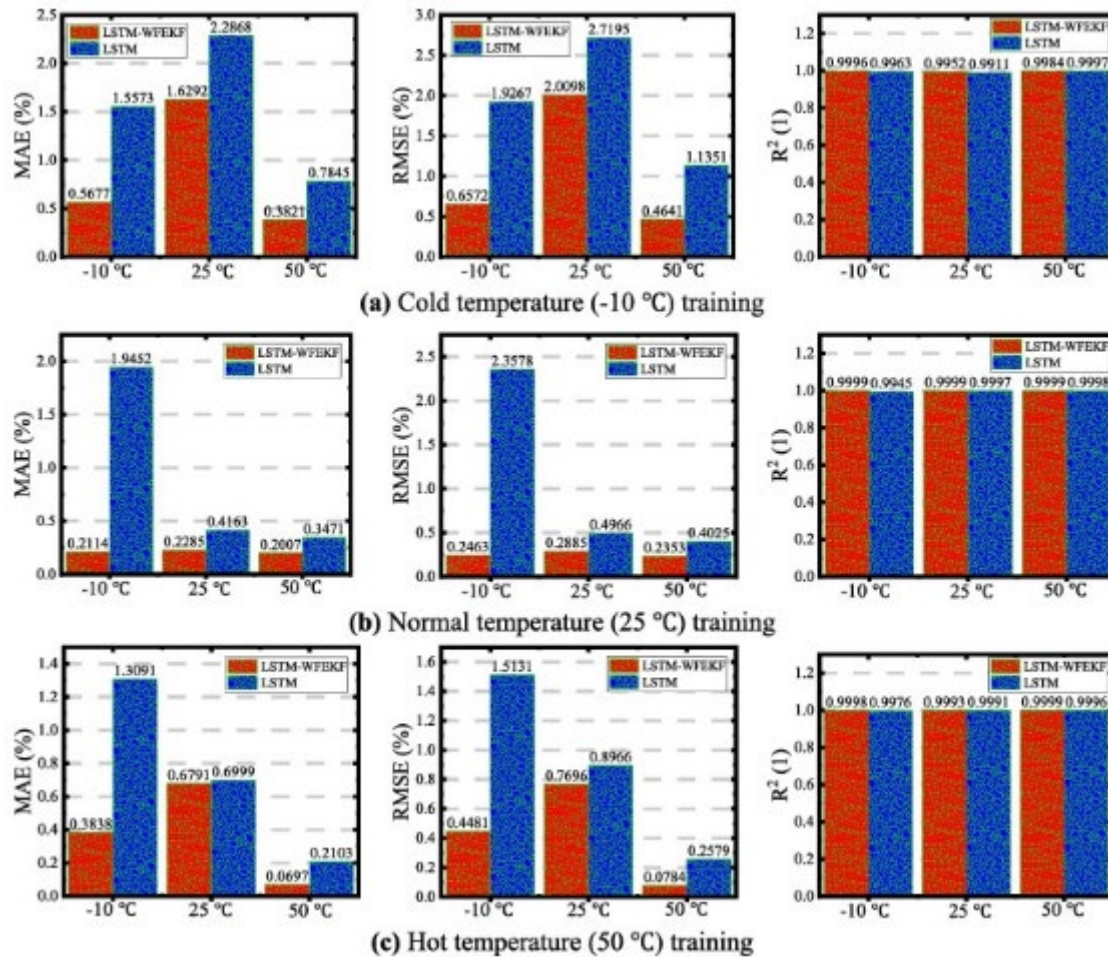


Fig. 11. Performance evaluation of the LSTM and LSTM-WFEKF models at different temperatures under the HPPC working condition.

Fig. 11 shows the evaluated performance of the LSTM and LSTMWFEKF models using the same training and testing sequence. It can be observed that the proposed hybrid LSTM-WFEKF model has smaller metric values compared to the LSTM model. The MAE and RMSE values verify the robustness and accuracy of the proposed hybrid LSTM-WFEKF model over the data-driven LSTM model. Under the HPPC working condition, it can be observed that the LSTM model has the overall best MAE, RMSE, and R2 values of 0.2103%, 0.2579%, and 99.96%, respectively, at training and testing temperatures of 50 °C and 50 °C, respectively. Meanwhile, the LSTM-WFEKF model has the overall best MAE, RMSE, and R2 values of 0.0697%, 0.0784%, and 99.99%, respectively, at the same training and testing temperatures. These results show the accuracy and robustness of the LSTM-WFEKF model with MAE and RMSE performance improvements of 66.86% and 66.90%, respectively. From the R2 values, it can also be observed that both models exhibit a high level of fitness to the actual SOC of the battery system.

The performance of the estimated SOC by the LSTM and LSTMWFEKF models under the DST working condition is critically evaluated using the MAE, RMSE, and R2 metrics, as presented in Fig. 12.

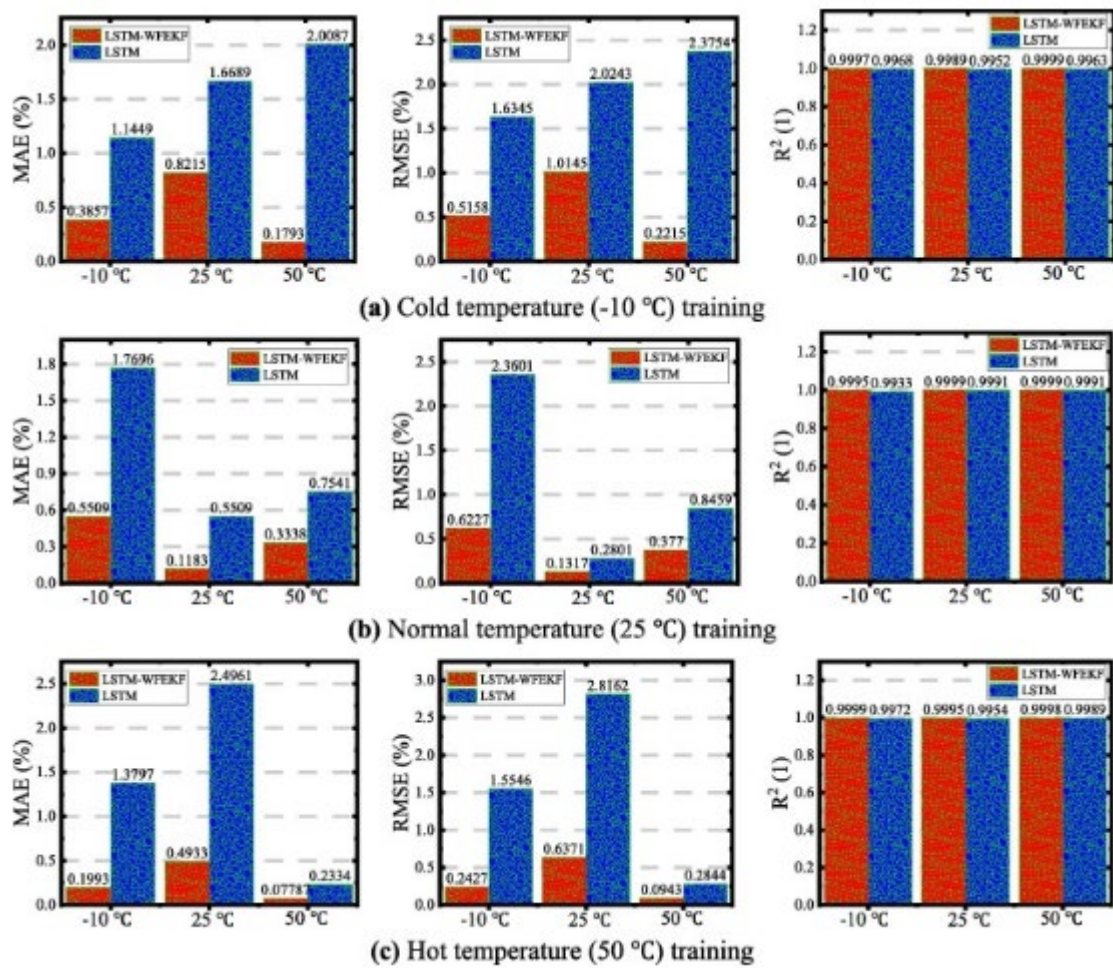


Fig. 12. Performance evaluation of the LSTM and LSTM-WFEKF models at different temperatures under the DST working condition.

Fig. 12 presents the evaluated performance of the LSTM and LSTMWFEKF models using the same training and testing sequence. Compared to the LSTM model, the proposed hybrid LSTM-WFEKF model has smaller metric values. The MAE and RMSE results show that the proposed hybrid LSTM-WFEKF model outperforms the data-driven LSTM model in terms of robustness and accuracy. Under the DST working condition, it can also be observed that the LSTM model has the overall best MAE, RMSE, and R<sup>2</sup> values of 0.2334%, 0.2844%, and 99.89%, respectively, using 50 °C training and 50 °C testing datasets. However, the hybrid LSTM-WFEKF model has the overall best MAE, RMSE, and R<sup>2</sup> values of 0.0778%, 0.0943%, and 99.98%, respectively, using the same training and testing temperatures. These results also indicate the LSTM-WFEKF model's accuracy and robustness, with MAE and RMSE performance improvements of 66.64% and 66.84%, respectively.

Furthermore, the critical performance evaluations of the SOC estimation by the LSTM and LSTM-WFEKF models under the BBDST working condition are presented in Fig. 13.

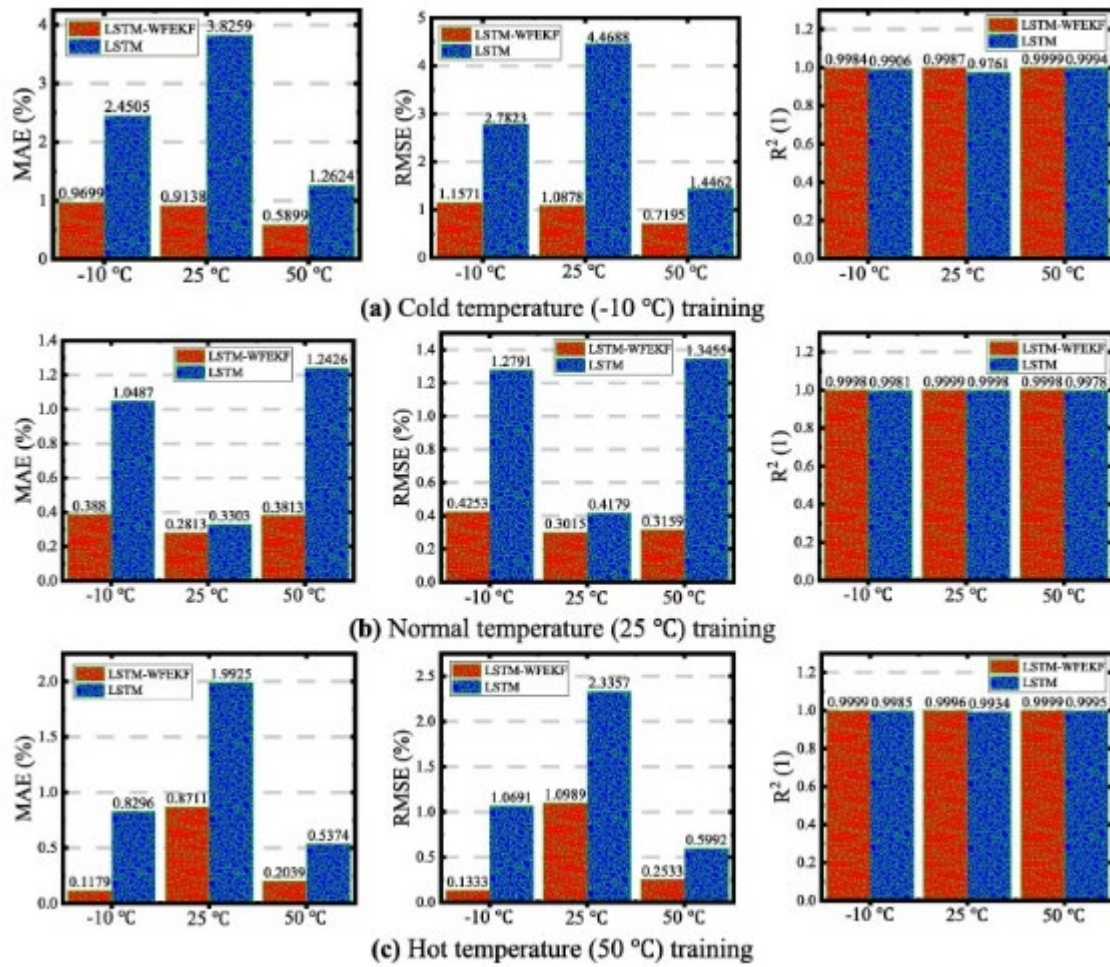


Fig. 13. Performance evaluation of the LSTM and LSTM-WFEKF models at different temperatures under the BBDST working condition.

Fig. 13 shows the critical performance evaluation of the LSTM and LSTM-WFEKF models using the same training and testing sequence and metrics. Also, the proposed hybrid LSTM-WFEKF model has smaller metric values compared to the LSTM model. In terms of robustness and accuracy, the MAE and RMSE results show that the proposed hybrid LSTM-WFEKF model outperforms the data-driven LSTM model. Using 25 °C training and 25 °C testing datasets, the LSTM model has the overall best MAE, RMSE, and  $R^2$  values of 0.3303%, 0.4179%, and 99.98%, respectively, under the BBDST working condition. However, the proposed LSTM-WFEKF model has the overall best MAE, RMSE, and  $R^2$  values of 0.1179%, 0.1333%, and 99.99%, respectively, using training and testing temperatures of 50 °C and -10 °C, respectively, showing good fitness than the LSTM model. These results demonstrate the accuracy and stability of the LSTM-WFEKF model, with MAE and RMSE performance enhancements of 64.31% and 68.10%, respectively.

Based on the metric values for the LSTM and LSTM-WFEKF models under the HPPC, DST, and BBDST working conditions, it can be observed that using a 25 °C (normal) training dataset ensures a more accurate estimation. Meanwhile, from the SOC estimation, the 50 °C (hot) training dataset has positive effects on the testing datasets to ensure less noisy SOC estimation, but the -10 °C (cold) training dataset has noisy effects on the estimates. Also, even though the LSTM-WFEKF model outperforms the established LSTM, it has low MAE and RMSE metrics and optimal fitness ( $R^2$ ) values, which verifies their robustness under different temperatures and working conditions.

### 3.3.3. Comparative performance evaluation of the proposed LSTM-WFEKF with other existing models

The proposed LSTM-WFEKF model is compared with other existing SOC estimation methods using the overall best metric values to evaluate their performance. In a total of seven case studies at different operating temperatures, including PSO-SRCKF [27], polynomial regression-based battery model-adaptive UKF (PRBM-AUKF) [28], fractional-order dual (FOD)-UKF [29], dynamic time warping (DTW) [66], and other optimal models are employed in comparison with the proposed LSTM-WFEKF model, as presented in Table 5.

Table 5. Comparative performance evaluation of the LSTM-WFEKF model with other existing models.

Models	Battery	Working conditions	Temperature	Overall best metric values
PSO-SRCKF [27]	LNCM4Ah	FUDS & DST	-10 & 60 °C	MAE = 0.95% RMSE = 1.03%
PRBM-AUKF [28]	LFP3.3Ah	Pulse discharge-charge test	-5-45 °C	RMSE = 0.46% MARPE = 1.27%
FOD-UKF [29]	L- NCM20Ah	OCV test & NEDC	0-40 °C	MAE = 0.55% RMSE = 0.91%
LSTM-ACKF [50]	LFP2.23Ah	FUDS & US06	10-50 °C	ME = 2.2% RMSE = 0.8%
GRU-TL [52]	L- NCM3.0Ah	FUDS, US06, & UDDS	32, 36, 42, & 50 °C	MAE = 0.853% RMSE = 1.115%
SSMPI [55]	LNCM2Ah	FUDS, US06, & BBDST	0, 25, & 45 °C	ME = 0.34% MAE = 0.664%
DTW [66]	LFP10Ah	Pulse discharge-charge test	5-30 °C	ME = 0.70% MAE = 0.40%
LSTM-WFEKF (Proposed in this paper)	LNCM70Ah	HPPC, DST, & BBDST	-10, 25, & 50 °C	MAE = 0.0697% RMSE = 0.0784% $R^2 = 99.9965\%$

In Table 5, using the overall best model performance under different temperatures and working conditions in the respective studies, it can be observed that the proposed LSTM-WFEKF model is superior and robust after comparing it with other existing SOC estimation models. The proposed LSTM-WFEKF model estimates the SOC with an overall best MAE, RMSE, and  $R^2$  values of 0.0697%, 0.0784%, and 99.9965%, respectively, at different temperatures of  $-10$ ,  $25$ , and  $50$  °C and under three complex working conditions. It can be observed that the SSMPPI model [55] is next by estimating the SOC with ME and MAE values of 0.34% and 0.664% at operating temperatures of  $0$ ,  $25$ , and  $45$  °C.

#### **4. Conclusion**

In this paper, an optimized LSTM-WFEKF model with wide temperature adaptation is proposed for the SOC estimation of lithium-ion batteries. Firstly, the input datasets are categorized based on the operating temperatures for EVs in the USABC manual: cold ( $-10$  °C), normal ( $25$  °C), and hot ( $50$  °C) temperatures and optimized with an attention mechanism to cross-train and test the LSTM model and study the effects of temperature on the SOC estimation through a TL mechanism. Secondly, the SOC estimated by the LSTM model is input into the WFEKF method, which introduces adaptive weighing and fading factors during the update of the posteriori state estimate and error covariance matrix, respectively, of the conventional EKF method to denoise and optimize the final SOC for each temperature variation under three complex working conditions. The results show that the training and testing temperature datasets have distinctive effects on SOC estimation. Also, the proposed LSTM-WFEKF model provides accurate convergence, low noise, and good end-of-discharge error correction ability with optimal accuracy compared to the LSTM model. It estimates the SOC with the overall best MAE, RMSE, and  $R^2$  values of 0.0697%, 0.0784%, and 99.9965%, respectively, under the HPPC working condition. Under the DST working condition, it estimates the SOC with an overall best MAE, RMSE, and  $R^2$  values of 0.0779%, 0.0943%, and 99.9842%, respectively. Finally, the proposed LSTM-WFEKF model estimates the SOC with an overall best MAE, RMSE, and  $R^2$  values of 0.1179%, 0.1333%, and 99.9819%, respectively, under the BBDST working condition. It further denoises and optimizes the final SOC to ensure a steady-state estimation for real-time BMS applications with wide temperature and working condition adaptation compared to other existing SOC estimation models. Finally, this paper concludes by proposing that the  $25$  °C training dataset ensures more accurate SOC estimation based on the MAE, RMSE, and  $R^2$  values under the HPPC, DST, and BBDST working conditions. Meanwhile, the training datasets at  $-10$  °C and  $50$  °C produce more and less noisy estimates, respectively. The proposed LSTMWFEKF model has wide temperature and working condition adaptability for real-time BMS applications in EVs.

In this paper, it is observed that the proposed WFEKF method produces a more accurate SOC estimation. However, it increases the total estimation time due to the adaptive adjustment of the weighing and fading factors, even though the attention mechanism is used to reduce the training and testing time of the LSTM model. Therefore, in our future work, we will focus on further reducing the total estimation time to study different aging levels and charge–discharge current rates at different temperatures and working conditions. Moreover, different battery chemistries will be considered and compared with other methods to enhance the practicality of the proposed LSTM-WFEKF model for optimal real-time BMS applications.

#### **Acknowledgment**

The work is supported by the National Natural Science Foundation of China (No. 62173281), China Scholarship Council (No. 201908515099), the Fund of Robot Technology used for Special Environment Key Laboratory of Sichuan Province (No. 18kftk03), and the Natural Science Foundation of Southwest University of Science and Technology (No. 17zx7110, 18zx7145).

## **References**

- [1] Li L, Ren Y, O'Regan K, Koleti UR, Kendrick E, Widanage WD, et al. Lithium-ion battery cathode and anode potential observer based on reduced-order electrochemical single particle model. *J Storage Mater* 2021;44:103324. <https://doi.org/10.1016/j.est.2021.103324>.
- [2] Sui X, He S, Vilsen SB, Meng J, Teodorescu R, Stroe D-I. A review of nonprobabilistic machine learning-based state of health estimation techniques for Lithium-ion battery. *Appl Energy* 2021;300:117346. <https://doi.org/10.1016/j.apenergy.2021.117346>.
- [3] Tran M-K, Mathew M, Janhunen S, Panchal S, Raahemifar K, Fraser R, et al. A comprehensive equivalent circuit model for lithium-ion batteries, incorporating the effects of state of health, state of charge, and temperature on model parameters. *J Storage Mater* 2021;43:103252. <https://doi.org/10.1016/j.est.2021.103252>.
- [4] Harding JR, Han B, Madden SB, Horn QC. Examining the performance of implantable grade lithium-ion cells after over-discharge and thermally accelerated aging. *Energies* 2022;15:1405. <https://doi.org/10.3390/en15041405>.
- [5] Park JH, Lee JH, Kim SJ, Lee IS. Real-time state of charge estimation for each cell of lithium battery pack using neural networks. *Appl Sci* 2020;10:8644. <https://doi.org/10.3390/app10238644>.
- [6] Takyi-Aninakwa P, Wang S, Zhang H, Li H, Xu W, Fernandez C. An optimized relevant long short-term memory-squared gain extended Kalman filter for the state of charge estimation of lithium-ion batteries. *Energy* 2022;260:125093. <https://doi.org/10.1016/j.energy.2022.125093>.
- [7] Liu C, Hu M, Jin G, Xu Y, Zhai J. State of power estimation of lithium-ion battery based on fractional-order equivalent circuit model. *J Storage Mater* 2021;41: 102954. <https://doi.org/10.1016/j.est.2021.102954>.
- [8] Miao Y, Gao Z. Estimation for state of charge of lithium-ion batteries by adaptive fractional-order unscented Kalman filters. *J Storage Mater* 2022;51:104396. <https://doi.org/10.1016/j.est.2022.104396>.
- [9] Chang C, Wu Y, Jiang J, Jiang Y, Tian A, Li T, et al. Prognostics of the state of health for lithium-ion battery packs in energy storage applications, *Energy*, 239. Part B 2022;122189. <https://doi.org/10.1016/j.energy.2021.122189>.
- [10] Takyi-Aninakwa P, Wang S, Zhang H, Appiah E, Bobobee ED, Fernandez C. A strong tracking adaptive fading-extended Kalman filter for the state of charge estimation of lithium-ion batteries. *Int J Energy Res* 2022;1–18. <https://doi.org/10.1002/er.8307>.
- [11] Lai X, Wang S, He L, Zhou L, Zheng Y. A hybrid state-of-charge estimation method based on credible increment for electric vehicle applications with large sensor and model errors. *J Storage Mater* 2020;27:101106. <https://doi.org/10.1016/j.est.2019.101106>.
- [12] McCarthy K, Gullapalli H, Ryan KM, Kennedy T. Electrochemical impedance correlation analysis for the estimation of Li-ion battery state of charge, state of health and internal temperature. *J Storage Mater* 2022;50:104608. <https://doi.org/10.1016/j.est.2022.104608>.

- [13] Jibhkate UN, Mujumdar UB. Development of low complexity open circuit voltage model for state of charge estimation with novel curve modification technique. *Electrochim Acta* 2022;429:140944. <https://doi.org/10.1016/j.electacta.2022.140944>.
- [14] Esser M, Rohde G, Rehtanz C. Electrochemical Impedance Spectroscopy Setup based on Standard Measurement Equipment. *J Power Sources* 2022;544:231869. <https://doi.org/10.1016/j.jpowsour.2022.231869>.
- [15] Kwak M, Lkhagvasuren B, Park J, You J. Parameter identification and SOC estimation of a battery under the hysteresis effect. *IEEE Trans Ind Electron* 2020; 67:9758–67.
- [16] Movassagh K, Raihan A, Balasingam B, Pattipati K. Critical look at coulomb counting approach for state of charge estimation in batteries. *Energies* 2021;14: 4074. <https://doi.org/10.3390/en14144074>.
- [17] Zhang R, Xia B, Li B, Cao L, Lai Y, Zheng W, et al. A study on the open circuit voltage and state of charge characterization of high-capacity lithium-ion battery under different temperature. *Energies* 2018;11:2408. <https://doi.org/10.3390/en11092408>.
- [18] Khaki B, Das P. An equivalent circuit model for vanadium redox batteries via hybrid extended Kalman filter and particle filter methods. *J Storage Mater* 2021; 39:102587. <https://doi.org/10.1016/j.est.2021.102587>.
- [19] Ge D, Zhang Z, Kong X, Wan Z. Online SoC estimation of lithium-ion batteries using a new sigma points Kalman filter. *Appl Sci* 2021;11(11797):1–22. <https://doi.org/10.3390/app112411797>.
- [20] Ling L, Sun D, Yu X, Huang R. State of charge estimation of lithium-ion batteries based on the probabilistic fusion of two kinds of cubature Kalman filters. *J Storage Mater* 2021;43:103070. <https://doi.org/10.1016/j.est.2021.103070>.
- [21] Rzepka B, Bischof S, Blank T. Implementing an extended Kalman filter for SOC estimation of a Li-ion battery with hysteresis: a step-by-step guide. *Energies* 2021; 14:3733. <https://doi.org/10.3390/en14133733>.
- [22] Xing J, Wu P. State of charge estimation of lithium-ion battery based on improved adaptive unscented Kalman filter. *Sustainability* 2021;13:5046. <https://doi.org/10.3390/su13095046>.
- [23] Lai X, Huang Y, Han X, Gu H, Zheng Y. A novel method for state of energy estimation of lithium-ion batteries using particle filter and extended Kalman filter. *J Storage Mater* 2021;43:103269. <https://doi.org/10.1016/j.est.2021.103269>.
- [24] Chen Z, Zhou J, Zhou F, Xu S. State-of-charge estimation of lithium-ion batteries based on improved H infinity filter algorithm and its novel equalization method. *J Cleaner Prod* 2021;290:125180. <https://doi.org/10.1016/j.jclepro.2020.125180>.
- [25] Oluwole OS, Zheng W, Chen J, Qiao Z. State of charge estimation of lithium-ion battery using an improved fractional-order extended Kalman filter. *J Storage Mater* 2022;49:104007. <https://doi.org/10.1016/j.est.2022.104007>.
- [26] Zhang S, Zhang C, Jiang S, Zhang X. A comparative study of different adaptive extended/unscented Kalman filters for lithium-ion battery state-of-charge estimation. *Energy* 2022;246:123423. <https://doi.org/10.1016/j.energy.2022.123423>.
- [27] Shen J, Ma W, Xiong J, Shu X, Zhang Y, Chen Z, et al. Alternative combined coestimation of state of charge and capacity for lithium-ion batteries in wide temperature scope. *Energy* 2022;244:123236. <https://doi.org/10.1016/j.energy.2022.123236>.

- [28] Hossain M, Haque ME, Arif MT. Kalman filtering techniques for the online model parameters and state of charge estimation of the Li-ion batteries: A comparative analysis. *J Storage Mater* 2022;51:104174. <https://doi.org/10.1016/j.est.2022.104174>.
- [29] Wu J, Fang C, Jin Z, Zhang L, Xing J. A multi-scale fractional-order dual unscented Kalman filter based parameter and state of charge joint estimation method of lithium-ion battery. *J Storage Mater* 2022;50:104666. <https://doi.org/10.1016/j.est.2022.104666>.
- [30] Fan X, Zhang W, Zhang C, Chen A, An F. SOC estimation of Li-ion battery using convolutional neural network with U-Net architecture. *Energy* 2022;256:124612. <https://doi.org/10.1016/j.energy.2022.124612>.
- [31] Wang Y, Chen Z. A framework for state-of-charge and remaining discharge time prediction using unscented particle filter. *Appl Energy* 2020;260:114324. <https://doi.org/10.1016/j.apenergy.2019.114324>.
- [32] Wang S, Takyi-Aninakwa P, Jin S, Yu C, Fernandez C, Stroe D-I. An improved feedforward-long short-term memory modeling method for the whole-life-cycle state of charge prediction of lithium-ion batteries considering current-voltage-temperature variation, *Energy*, 254. Part A 2022;124224. <https://doi.org/10.1016/j.energy.2022.124224>.
- [33] Chen Z, Sun H, Dong G, Wei J, Wu J. Particle filter-based state-of-charge estimation and remaining-dischargeable-time prediction method for lithium-ion batteries. *J Power Sources* 2019;414:158–66.
- [34] Roman-Ramírez LA, Marco J. Design of experiments applied to lithium-ion batteries: A literature review. *Appl Energy* 2022;320:119305. <https://doi.org/10.1016/j.apenergy.2022.119305>.
- [35] Wang Q, Ye M, Wei M, Lian G, Wu C. Co-estimation of state of charge and capacity for lithium-ion battery based on recurrent neural network and support vector machine. *Energy Rep* 2021;7:7323–32. <https://doi.org/10.1016/j.egyr.2021.10.095>.
- [36] Wei Z, Hu J, Li Y, He H, Li W, Sauer DU. Hierarchical soft measurement of load current and state of charge for future smart lithium-ion batteries. *Appl Energy* 2022;307:118246. <https://doi.org/10.1016/j.apenergy.2021.118246>.
- [37] Xia L., Wang S., Yu C., Fan Y., Li B., Xie Y., Joint estimation of the state-of-energy and state-of-charge of lithium-ion batteries under a wide temperature range based on the fusion modeling and online parameter prediction, *Journal of Energy Storage*, 52, Part C, 2022, 105010, <https://doi.org/10.1016/j.est.2022.105010>.
- [38] Narayanan SSS, Thangavel S. Machine learning-based model development for battery state of charge–open circuit voltage relationship using regression techniques. *J Storage Mater* 2022;49:104098. <https://doi.org/10.1016/j.est.2022.104098>.
- [39] Hong J, Wang Z, Chen W, Wang L-Y, Qu C. Online joint-prediction of multi-forward-step battery SOC using LSTM neural networks and multiple linear regression for real-world electric vehicles. *J Storage Mater* 2020;30:101459. <https://doi.org/10.1016/j.est.2020.101459>.
- [40] Deng Z, Hu X, Lin X, Che Y, Xu L, Guo W. Data-driven state of charge estimation for lithium-ion battery packs based on Gaussian process regression. *Energy* 2020;205: 118000. <https://doi.org/10.1016/j.energy.2020.118000>.
- [41] Ma L, Hu C, Cheng F. State of charge and state of energy estimation for lithium-ion batteries based on a long short-term memory neural network. *J Storage Mater* 2021;37:102440. <https://doi.org/10.1016/j.est.2021.102440>.

- [42] Hannan MA, Lipu MSH, Hussain A, Ker PJ, Mahlia TMI, Mansor M, et al. Toward enhanced state of charge estimation of lithium-ion batteries using optimized machine learning techniques. *Sci Rep* 2020;10:4687. <https://doi.org/10.1038/s41598-020-61464-7>.
- [43] Zuo H, Zhang B, Huang Z, Wei K, Zhu H, Tan J. Effect analysis on SOC values of the power lithium manganate battery during discharging process and its intelligent estimation, *Energy*, 238. Part B 2022;121854. <https://doi.org/10.1016/j.energy.2021.121854>.
- [44] Chen J, Feng X, Jiang L, Zhu Q. State of charge estimation of lithium-ion battery using denoising autoencoder and gated recurrent unit recurrent neural network. *Energy* 2021;227:120451. <https://doi.org/10.1016/j.energy.2021.120451>.
- [45] Gong Q, Wang P, Cheng Z. A novel deep neural network model for estimating the state of charge of lithium-ion battery. *J Storage Mater* 2022;54:105308. <https://doi.org/10.1016/j.est.2022.105308>.
- [46] Ren X, Liu S, Yu X, Dong X. A method for state-of-charge estimation of lithium-ion batteries based on PSO-LSTM. *Energy* 2021;234:121236. <https://doi.org/10.1016/j.energy.2021.121236>.
- [47] Zheng X, Zhang Z. State of charge estimation at different temperatures based on dynamic thermal model for lithium-ion batteries. *J Storage Mater* 2022;48:104011. <https://doi.org/10.1016/j.est.2022.104011>.
- [48] Oyewole I, Chehade A, Kim Y. A controllable deep transfer learning network with multiple domain adaptation for battery state-of-charge estimation. *Appl Energy* 2022;312:118726. <https://doi.org/10.1016/j.apenergy.2022.118726>.
- [49] Yang F, Li W, Li C, Miao Q. State-of-charge estimation of lithium-ion batteries based on gated recurrent neural network. *Energy* 2019;175:66–75. <https://doi.org/10.1016/j.energy.2019.03.059>.
- [50] Tian Y, Lai R, Li X, Xiang L, Tian J. A combined method for state-of-charge estimation for lithium-ion batteries using a long short-term memory network and an adaptive cubature Kalman filter. *Appl Energy* 2020;265:114789. <https://doi.org/10.1016/j.apenergy.2020.114789>.
- [51] Bian C, He H, Yang S. Stacked bidirectional long short-term memory networks for state-of-charge estimation of lithium-ion batteries. *Energy* 2020;191:116538. <https://doi.org/10.1016/j.energy.2019.116538>.
- [52] Yang F, Zhang S, Li W, Miao Q. State-of-charge estimation of lithium-ion batteries using LSTM and UKF. *Energy* 2020;201:117664. <https://doi.org/10.1016/j.energy.2020.117664>.
- [53] Fasahat M, Manthouri M. State of charge estimation of lithium-ion batteries using hybrid autoencoder and long short-term memory neural networks. *J Power Sources* 2020;469:228375. <https://doi.org/10.1016/j.jpowsour.2020.228375>.
- [54] Wang YX, Chen Z, Zhang W. Lithium-ion battery state-of-charge estimation for small target sample sets using the improved GRU-based transfer learning. *Energy* 2022;244:123178. <https://doi.org/10.1016/j.energy.2022.123178>.
- [55] Ma L, Wang Z, Yang F, Cheng Y, Lu C, Tao L, et al. Robust state of charge estimation based on a sequence-to-sequence mapping model with process information. *J Power Sources* 2020;474:228691. <https://doi.org/10.1016/j.jpowsour.2020.228691>.
- [56] Ruiz V., Di Persio F (Co)., JRC Technical Reports, Standards for the performance and durability assessment of electric vehicle batteries (Possible performance criteria for an Ecodesign Regulation), 2018.

- [57] US Department of Energy, USABC ELECTRIC VEHICLE BATTERY TEST PROCEDURES MANUAL (usabc\_manual\_rev2), January 1996.
- [58] Yang N, Song Z, Hofmann H, Sun J. Robust State of Health estimation of lithiumion batteries using convolutional neural network and random forest. *J Storage Mater* 2022;48:103857. <https://doi.org/10.1016/j.est.2021.103857>.
- [59] Chen J., Zhang Y., Li W., Cheng W., Zhu Q., State of charge estimation for lithiumion batteries using gated recurrent unit recurrent neural network and adaptive Kalman filter, *Journal of Energy Storage*, 55, Part A, 2022, 105396, <https://doi.org/10.1016/j.est.2022.105396>.
- [60] Liu Y., He Y., Bian H., Guo W., Zhang X., A review of lithium-ion battery state of charge estimation based on deep learning: Directions for improvement and future trends, *Journal of Energy Storage*, 52, Part A, 2022, 104664, <https://doi.org/10.1016/j.est.2022.104664>.
- [61] Ni Z., Xiu X., Yang Y., Towards efficient state of charge estimation of lithium-ion batteries using canonical correlation analysis, *Energy*, 254, Part C, 2022, 124415, <https://doi.org/10.1016/j.energy.2022.124415>.
- [62] Manoharan A., Begam K.M., Aparow V.R., Sooriamoorthy D., Artificial neural networks, gradient boosting and support vector machines for electric vehicle battery state estimation: A review, *Journal of Energy Storage*, 55, Part A, 2022, 105384, <https://doi.org/10.1016/j.est.2022.105384>.
- [63] Deng Z, Lin X, Cai J, Hu X. Battery health estimation with degradation pattern recognition and transfer learning. *J Power Sources* 2022;525:231027. <https://doi.org/10.1016/j.jpowsour.2022.231027>.
- [64] Zhang S, Zhang X. A multi time-scale framework for state-of-charge and capacity estimation of lithium-ion battery under optimal operating temperature range. *J Storage Mater* 2021;35:102325. <https://doi.org/10.1016/j.est.2021.102325>.
- [65] Jiang C, Wang S, Wu B, Fernandez C, Xiong X, Coffie-Ken J. A state-of-charge estimation method of the power lithium-ion battery in complex conditions based on adaptive square root extended Kalman filter. *Energy* 2021;219:119603. <https://doi.org/10.1016/j.energy.2020.119603>.
- [66] Li X, Xiao L, Geng G, Jiang Q. Temperature characterization based state-of-charge estimation for pouch lithium-ion battery. *J Power Sources* 2022;535:231441. <https://doi.org/10.1016/j.jpowsour.2022.231441>.